The Astrophysical Journal, 697:436–451, 2009 May 20 doi:10.1088/0004-637X/697/1/436

THE *XMM* CLUSTER SURVEY: GALAXY MORPHOLOGIES AND THE COLOR–MAGNITUDE RELATION IN XMMXCS J2215.9−1738 AT $z = 1.46$

Matt Hilton[1,2,3], S. Adam Stanford[4,5], John P. Stott[3], Chris A. Collins[3], Ben Hoyle[6], Michael Davidson[7], Mark Hosmer[8], Scott T. Kay[9], Andrew R. Liddle[8], Ed Lloyd-Davies[8], Robert G. Mann[7], Nicola Mehrtens[8], Christopher J. Miller[10], Robert C. Nichol[6], A. Kathy Romer[8], Kivanc Sabirli[8], Martin Sahlén[8], Pedro T. P. Viana[11,12], Michael J. West[13], Kyle Barbary[14,15], Kyle S. Dawson[16], Joshua Meyers[14,15], Saul Perlmutter[14,15], David Rubin[14,15], and Nao Suzuki[14]

[1] Astrophysics & Cosmology Research Unit, School of Mathematical Sciences, University of KwaZulu-Natal, Private Bag X54001, Durban 4000, South Africa; hiltonm@ukzn.ac.za
[2] South African Astronomical Observatory, P.O. Box 9, Observatory, 7935, Cape Town, South Africa
[3] Astrophysics Research Institute, Liverpool John Moores University, Twelve Quays House, Egerton Wharf, Birkenhead CH41 1LD, UK
[4] University of California, Davis, CA 95616, USA
[5] Institute of Geophysics and Planetary Physics, Lawrence Livermore National Laboratory, Livermore, CA 94551, USA
[6] Institute of Cosmology and Gravitation, University of Portsmouth, Portsmouth PO1 2EG, UK
[7] Institute of Astronomy, University of Edinburgh, Blackford Hill, Edinburgh EH9 9HJ, UK
[8] Astronomy Centre, University of Sussex, Falmer, Brighton BN1 9QH, UK
[9] University of Manchester, Jodrell Bank Observatory, Macclesfield, Cheshire SK11 9DL, UK
[10] Cerro-Tololo Inter-American Observatory, National Optical Astronomy Observatory, 950 North Cherry Avenue, Tucson, AZ 85719, USA
[11] Departmento de Matemática Aplicada da Faculdade de Ciências da Universidade do Porto, Rua do Campo Alegre 687, 4169-007, Portugal
[12] Centro de Astrofísica da Universidade do Porto, Rua das Estrelas, 4150-762 Porto, Portugal
[13] European Southern Observatory, Alonso de Córdova 3107, Vitacura, Casilla 19001, Santiago 19, Chile
[14] E. O. Lawrence Berkeley National Laboratory, 1 Cyclotron Road, Berkeley, CA 94720, USA
[15] Department of Physics, University of California Berkeley, Berkeley, CA 94720-7300, USA
[16] Department of Physics and Astronomy, University of Utah, Salt Lake City, UT 84112, USA
Received 2008 December 1; accepted 2009 March 11; published 2009 May 1

ABSTRACT

We present a study of the morphological fractions and color–magnitude relation (CMR) in the most distant X-ray selected galaxy cluster currently known, XMMXCS J2215.9−1738 at $z = 1.46$, using a combination of optical imaging data obtained with the *Hubble Space Telescope* Advanced Camera for Surveys, and infrared data from the Multi-Object Infrared Camera and Spectrograph, mounted on the 8.2 m Subaru telescope. We find that the morphological mix of the cluster galaxy population is similar to clusters at $z \sim 1$. Within the central 0.5 Mpc, approximately ∼62% of the galaxies identified as likely cluster members are ellipticals or S0s; and ∼38% are spirals or irregulars. Therefore, early-type galaxies were already entrenched as the dominant galaxy population in at least some clusters approximately ∼ 4.5 Gyr after the big bang. We measure the CMRs for the early-type galaxies, finding that the slope in the z_{850}–J relation is consistent with that measured in the Coma cluster, some ∼9 Gyr earlier, although the uncertainty is large. In contrast, the measured intrinsic scatter about the CMR is more than three times the value measured in Coma, after conversion to rest-frame $U-V$. From comparison with stellar population synthesis models, the intrinsic scatter measurements imply mean luminosity-weighted ages for the early-type galaxies in J2215.9−1738 of ≈3 Gyr, corresponding to the major epoch of star formation coming to an end at $z_f \approx 3$–5. We find that the cluster exhibits evidence of the "downsizing" phenomenon: the fraction of faint cluster members on the red sequence expressed using the Dwarf-to-Giant Ratio (DGR) is 0.32 ± 0.18 within a radius of $0.5R_{200}$. This is consistent with extrapolation of the redshift evolution of the DGR seen in cluster samples at $z < 1$. In contrast to observations of some other $z > 1$ clusters, we find a lack of very bright galaxies within the cluster.

Key words: galaxies: clusters: individual (XMMXCS J2215.9−1738) – galaxies: elliptical and lenticular, cD – galaxies: evolution – X-rays: galaxies: clusters

1. INTRODUCTION

The galaxy populations of clusters are dominated by galaxies of early morphological type, ellipticals, and S0s, which form a tight color–magnitude relation (CMR) or "red sequence." For decades, this relation was interpreted as evidence that the stars in early-type galaxies in clusters are uniformly old, being formed at redshift $z_f > 2$, with the slope of the relation being primarily due to a mass–metallicity relation (Larson 1974; Tinsley 1978; Gallazzi et al. 2006). The alternative interpretation of the CMR as being predominantly an age sequence was conclusively ruled out by observations of clusters at $z \lesssim 0.4$, which showed that the slope of the CMR evolves little with redshift (Kodama & Arimoto 1997).

A number of studies of clusters conducted with the *Hubble Space Telescope* (*HST*) have shown that the CMR of elliptical galaxies remains well established at progressively higher redshifts (e.g., Ellis et al. 1997; Stanford et al. 1998; van Dokkum et al. 2000), at least up to $z \sim 1.3$ (van Dokkum et al. 2001; Blakeslee et al. 2003; Mei et al. 2006b). The only study to date of the CMR in a cluster at $z = 1.4$ is consistent with this picture (Lidman et al. 2008). Measurements of the intrinsic scatter about the CMR can be used to constrain the ages of the constituent stellar populations of cluster early-type galaxies, and indicate that major epoch of star formation in clusters was completed at $z > 2$ (e.g., Bower et al. 1992; Blakeslee et al. 2003; Mei et al. 2009). Studies of the fundamental plane of elliptical galaxies up to high redshift similarly indicate that the bulk of stellar

populations in elliptical galaxies were formed at $z > 2$ (e.g., van Dokkum & Stanford 2003; Holden et al. 2005; Jørgensen et al. 2006; van Dokkum & van der Marel 2007).

These observations are consistent with a simple formation scenario for elliptical galaxies, in which they formed the bulk of their stellar mass in a single event at high redshift, and evolved passively thereafter. However, the latest semianalytic models of galaxy formation, constructed within the hierarchical formation paradigm, are also able to successfully reproduce the old ages of stellar populations in elliptical galaxies (De Lucia et al. 2006; Menci et al. 2008).

Recent observations over a wide range in redshift in both clusters and the field have revealed that star formation appears to be completed earlier in higher-mass galaxies than in low-mass galaxies, a phenomenon dubbed "downsizing" (Cowie et al. 1996). In color–magnitude diagrams (CMDs) of high-redshift clusters, this effect manifests itself as a deficit of faint galaxies on the red sequence in comparison to clusters observed at lower redshift (e.g., De Lucia et al. 2004, 2007; Stott et al. 2007), and may have an environmental dependence in the sense that the faint end of the CMR is populated at earlier times in denser regions, such as in the cluster cores, compared to low-density regions such as groups (e.g., Tanaka et al. 2005, 2008; Gilbank et al. 2008).

This could be explained qualitatively by a scenario in which the faint end of the red sequence is being built up by the transformation of star forming, spiral galaxies into passively evolving S0s as redshift increases. Up to $z \sim 1$, studies of magnitude-limited samples of cluster galaxies have revealed that the elliptical galaxy fraction within clusters is found to remain roughly constant, while the fraction of S0 galaxies decreases, with a corresponding increase in the fraction of spiral and irregular galaxies (Dressler et al. 1997; Smith et al. 2005; Postman et al. 2005). When considering stellar mass-limited samples, it has been found that the fraction of massive, early-type galaxies as a whole remains roughly constant, at least up to $z \approx 0.8$ (Holden et al. 2006, 2007; van der Wel et al. 2007). This suggests that the much stronger evolution seen in magnitude-limited samples is dominated by fainter, lower-mass (sub-M^* in the galaxy stellar mass function) galaxies. It should be noted that at the current time the evidence for downsizing within the centers of rich clusters is still somewhat contentious (Andreon 2008; Crawford et al. 2009).

In this paper, we present a study of the galaxy morphologies and CMR in XMMXCS J2215.9−1738 at $z = 1.46$ (Stanford et al. 2006; Hilton et al. 2007), the most distant X-ray selected galaxy cluster currently known. To date, only five other spectroscopically confirmed clusters are known at $z > 1.3$, XMMU J2235.3−2557 at $z = 1.39$, discovered serendipitously with *XMM-Newton* (Mullis et al. 2005); three clusters at $z = 1.33$–1.41 from the Infrared Array Camera (IRAC) Shallow Cluster Survey (ISCS; Eisenhardt et al. 2008; Stanford et al. 2005); and the $z = 1.335$ cluster J003550−431224, discovered by the *Spitzer* Adaptation of the Red-sequence Cluster Survey (SpARCS; Wilson et al. 2008).

J2215.9−1738 was discovered as part of the ongoing optical follow-up campaign to the *XMM* Cluster Survey (XCS[17]; Romer et al. 2001), which has the primary aim of constraining the cosmological parameters through measuring the evolution of the cluster mass function with redshift. Predictions for the expected cosmological constraints that are expected to be achieved by the full survey can be found in Sahlén et al. (2009). J2215.9−1738 has X-ray luminosity $L_X = 4.39^{+0.46}_{-0.37} \times 10^{44}$ erg s^{-1}, temperature $T = 7.4^{+1.6}_{-1.1}$ keV (Stanford et al. 2006), and velocity dispersion $\sigma_v = 580 \pm 140$ km s^{-1} (Hilton et al. 2007). There is mild evidence that the cluster velocity distribution is bimodal, which, if confirmed by further spectroscopic observations, would indicate that the cluster is undergoing a merger close to the line of sight (Hilton et al. 2007).

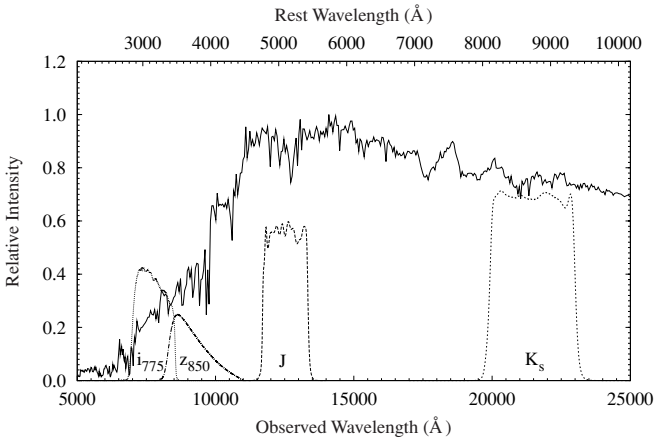

Figure 1. Response curves for the ACS (i_{775}, z_{850}) and MOIRCS (J, K_s) filters used in this study. The solid line is a Bruzual & Charlot (2003) model spectrum of a galaxy with solar metallicity, Salpeter (1955) IMF, formed at redshift $z_f = 4.5$ in a 0.1 Gyr burst of star formation, as it would be observed at the cluster redshift of $z = 1.46$. The near-infrared data are essential to bracket the 4000 Å break in early-type galaxies at this redshift.

The structure of this paper is as follows. We begin by describing the observations and data reduction in Section 2. In Section 3, we describe our photometric measurements, morphological classification, and photometric redshift selection of the cluster members. We present the morphological fractions, fits to the CMR, and inferred ages for the stellar populations of the early-type galaxies in Section 4. Finally, we discuss our findings in comparison with previous work in Section 5.

We assume a concordance cosmology of $\Omega_m = 0.3$, $\Omega_\Lambda = 0.7$, and $H_0 = 70$ km s^{-1} Mpc^{-1} throughout, where Ω_Λ is the energy density associated with a cosmological constant.

2. OBSERVATIONS AND DATA REDUCTION

For our study of the galaxy populations of J2215.9−1738, we use a combination of optical data in the i_{775} and z_{850} bands obtained with the *HST* Advanced Camera for Surveys (ACS; Ford et al. 2003), and near-infrared data in the J and K_s bands taken using the Multi-Object Infrared Camera and Spectrograph (MOIRCS; Ichikawa et al. 2006) on the 8.2 m Subaru telescope at the summit of Mauna Kea, Hawaii. As shown in Figure 1, at the cluster redshift of $z = 1.46$ the optical data lies blueward of the 4000 Å break, and therefore near-infrared data are essential to provide a color which is able to separate the cluster red sequence from bluer, star-forming galaxies. The z_{850}–J color at the cluster redshift of $z = 1.46$ roughly corresponds to rest-frame $U-V$, while z_{850}–K_s is roughly equivalent to rest-frame $U-z$.

Figure 2 presents a color-composite (z_{850}, J, K_s) image of the cluster. It is apparent from Figure 2 that J2215.9−1738 lacks an obvious brightest cluster galaxy (BCG), in contrast with the only other similarly high-redshift X-ray selected cluster currently known, XMMU J2235.3−2557 at $z = 1.39$ (Lidman et al. 2008;

[17] http://www.xcs-home.org

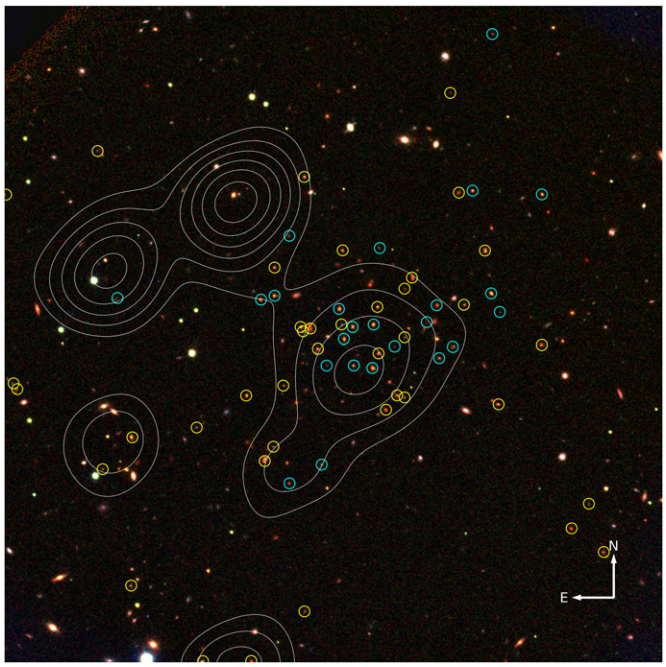

Figure 2. Color-composite (z_{850}, J, K_s) using the ACS and MOIRCS imaging data presented in this paper, centered on the cluster X-ray coordinates of $22^h15^m58^s.5$, $-17°38'02''.5$ (J2000). The image is 3.′04 on a side. The ACS z_{850} image has been degraded to match the 0.″5 resolution of the MOIRCS J, K_s imaging. X-ray contours are overlaid in white; cyan points indicate spectroscopically confirmed cluster members; yellow points indicate additional cluster members selected using photometric redshifts.

see also Collins et al. 2009). Similarly, the galaxy distribution is much less compact in J2215.9−1738 than in J2235.3−2557.

We now describe the observations and data reduction performed for each instrument in turn.

2.1. Hubble Space Telescope

J2215.9−1738 was observed using the ACS Wide Field Channel (WFC) as part of a program designed to place constraints on the dark energy through observations of high-redshift Type Ia supernovae.[18] The field of view of the ACS WFC is approximately 3.′4 × 3.′4, and the pixel scale of the detectors is 0.″05 per pixel. A detailed description of the ACS observations is presented in Dawson et al. (2008). A total of 3320 s of exposure was obtained in i_{775} across 12 frames. In z_{850}, 16,935 s of exposure was obtained in 64 frames. In both cases, the final stacked images were created using the `MULTIDRIZZLE` `PyRAF` task.[19]

2.2. Subaru

J2215.9−1738 was observed with MOIRCS in photometric conditions on UT 2007 August 8. The observations were carried out in service mode. The field of view of MOIRCS is 4′ × 7′, which is imaged at a resolution of 0.″117 per pixel on to a pair of 2048 × 2048 HAWAII-2 detector arrays. Unfortunately, one of the detector arrays was inoperable at the time our observations were carried out. Our observations were designed to place the target cluster at the center of the second, working detector array. We performed imaging in the J and K_s bands, using a nine-point circular dither pattern of radius 25″ to ensure good sky subtraction. We obtained a total of 1485 s of integration in J, for an individual frame time of 165 s at each dither position. In the K_s band, the total integration time was 1242 s, achieved by co-adding 3 × 46 s exposures at each dither position. The observations were obtained at airmass ≈1.3. The seeing was excellent, at ≈0.″5 in both J and K_s.

The data were reduced using the `MCSRED` package for the `IRAF`[20] environment in the standard manner: the individual dither frames were flat-fielded, sky-subtracted, corrected for distortion caused by the optical design of MOIRCS, and registered to a common pixel coordinate system. The final science images were created from the 3σ clipped mean of the dither frames.

3. ANALYSIS

3.1. Photometry

As most of our ACS data were obtained before UT 2006 July 4, we adopted AB photometric zero points in the i_{775} and z_{850} ACS bands of 25.678 and 24.867, respectively.[21] After this date, the ACS photometric zero points changed due to a change in the temperature of CCDs: frames obtained after this change occurred were adjusted to match the above zero points. During the MOIRCS observations, we obtained imaging of several photometric standards from the UKIRT faint standards list. The zero points we determined in the J and K_s bands are 26.435 ± 0.007 and 25.900 ± 0.010 on the Vega system, respectively. For the near-infrared data, we adopt conversions to the AB magnitude system (Oke 1974) of $J(\mathrm{AB}) = \mathrm{J(Vega)} + 0.943$ and $K_s(\mathrm{AB}) = K_s(\mathrm{Vega}) + 1.86$ (Tokunaga & Vacca 2005). All magnitudes quoted throughout the rest of this paper are on the AB system, unless stated otherwise.

To measure accurate colors for the galaxies in J2215.9−1738, we need to perform measurements through a consistent set of photometric apertures. We used the `SEXTRACTOR` package (Bertin & Arnouts 1996) in dual image mode to achieve this, where objects are detected and apertures are defined using the first image, while photometry is performed on the second image. We chose to use the MOIRCS K_s image as the detection image. As the ACS and MOIRCS imaging data have different angular and pixel resolution, some additional processing was required prior to performing the photometry.

First, we trimmed the ACS and MOIRCS images to cover a common area of dimensions 3.′04 × 3.′04, centered on the cluster X-ray position. This area encloses the overlapping ACS coverage from the individual dither frames, rejecting higher noise regions at the edges covered by fewer ACS pointings. We then scaled the MOIRCS images from their native pixel scale of 0.″117 per pixel to the ACS pixel scale of 0.″05 per pixel, interpolating using a third-order spline polynomial. The MOIRCS images were then registered to the ACS images to pixel accuracy. Finally, the ACS images were matched to the 0.″5 angular resolution of the MOIRCS images by convolution with a Gaussian filter with $\sigma = 4.0$ pixels.

To estimate the photometric errors in each band, we constructed rms images for use as weight images by `SEXTRACTOR`.

[18] Based on observations made with the NASA/ESA *HST*, obtained from the data archive at the Space Telescope Institute. STScI is operated by the association of Universities for Research in Astronomy, Inc. under the NASA contract NAS 5-26555. The observations are associated with program 10496.

[19] http://www.stsci.edu/resources/software_hardware/pyraf/stsci_python.

[20] IRAF is distributed by the National Optical Astronomy Observatories, which is operated by the Association of Universities for Research in Astronomy, Inc., under cooperative agreement with the National Science Foundation.

[21] See http://www.stsci.edu/hst/acs/analysis/zeropoints.

For the MOIRCS images, we used the rms images produced by the MCSRED data reduction package—these are simply the standard deviation at each pixel derived from the nine individual dither frames. For the ACS images, the rms images were constructed from the drizzled science images and the exposure time maps output by the MULTIDRIZZLE task, taking into account the photon statistics and the detector read noise. The drizzling process used to make the final ACS science images correlates the pixel-to-pixel noise, which, if ignored, would lead to underestimated photometric errors. We corrected for this effect following the methodology outlined in the appendix of Casertano et al. (2000).

The effect of the interpolation operations on the photometry from the MOIRCS images was tested by cross matching catalogs constructed at the native MOIRCS pixel scale, with catalogs made from the images resampled to match the ACS pixel scale. Objects were matched between each catalog within a 0.″5 radius and the 1.″0 aperture magnitudes were compared. We found that the median magnitude difference between the two catalogs was ≈0.001 for $J, K_s < 24$. We decided to treat the scatter between the catalogs as an additional source of uncertainty: we fitted an exponential model to the scatter as a function of magnitude, applied this model to the J, K_s aperture magnitudes in the catalog constructed at the ACS pixel resolution, and added the results in quadrature to the photometric errors output by SEXTRACTOR. The increase in the J and K_s aperture magnitude uncertainties resulting from this procedure is small, <0.04 mag at $J, K_s < 24$.

To classify objects as stars and galaxies, we constructed a second set of catalogs in the manner described above, with the exception that the ACS images were not matched to the 0.″5 resolution of the MOIRCS images, and instead were read into SEXTRACTOR at their native ≈0.″09 angular resolution. We used the neural-network based star-galaxy classification provided by SEXTRACTOR (CLASS_STAR) to determine the object types. We classify all objects with CLASS_STAR < 0.9 as measured in the z_{850} image as galaxies; all other objects are assumed to be stars. We chose to carry out the classification in the z_{850} band, because the z_{850} image is significantly deeper than the i_{775} image, reaching an approximate 5σ limiting magnitude of ≈26.0 for galaxies, compared to ≈25.1 for the i_{775} image (estimated from the photometric uncertainties).

We corrected the photometry for the effect of Galactic extinction using the dust maps and software of Schlegel et al. (1998). In all that follows, SEXTRACTOR MAG_AUTO magnitudes were adopted as measurements of total galaxy magnitudes, and colors were measured in 1.″0 diameter circular apertures, equal to twice the seeing of the MOIRCS images. This is comparable to the typical diameter of the cluster member galaxies.

Note that we do not attempt to correct the photometry of objects blended as a consequence of performing the object detection in the K_s band. Only a small number of such objects are seen, perhaps due to the galaxy distribution in J2215.9−1738 being less compact than other similarly high-redshift clusters, as noted in Section 2. As shown in Section 4.1, this has a negligible effect on our results.

3.2. Morphologies

Morphological classification was performed on all 201 galaxies with magnitudes brighter than $z_{850} \leqslant 24$, by visual inspection of the z_{850}-band imaging data. This is ∼2 mag brighter than the approximate 5σ mag limit of the z_{850}-band image. Due to the high redshift of J2215.9−1738, the morphological classification was carried out in the rest-frame U band, rather than the traditional B band (e.g., Postman et al. 2005). Furthermore, the typical diameter of the cluster member galaxies in the ACS imaging is <20 pixels, making detailed morphological classification on the traditional Hubble system difficult. For these reasons, we chose to place the galaxies into four broad morphological bins: elliptical (E; corresponding to E1–E9 on the traditional Hubble system), lenticular (S0), spiral (Sp; Sa−Sd, SBa−SBd on the traditional Hubble system) or irregular (Irr).

The classification was carried out on the complete sample by a team of five classifiers (CAC, MH, BH, SAS, JPS). Each galaxy in the sample was examined by means of a 150 pixel on a side postage stamp image, centered on the galaxy in question. No further information on the galaxy to be classified (e.g., position, redshift, color, or magnitude) was provided during the classification process, in order to ensure that the classification was determined strictly on the evidence of the imaging data alone, guarding against potential biases. The same training set of galaxy images, constructed from the Postman et al. (2005) study of galaxy morphologies in $0.8 < z < 1.3$ clusters, was provided to each classifier.

We found there was generally good agreement on the morphological classification of the individual galaxies among the five classifiers: majority agreement (i.e., >50% of the votes cast by the classifiers were for a particular morphology) was reached for 85% of the sample. Agreement by >2/3 of the classifiers was reached for 67% of the sample. We estimated the rms scatter between the morphological fractions determined by each classifier and adopted this as our estimate of the morphological classification error, used in Section 4.1. For the elliptical galaxy fraction, we measure a scatter of $\sigma_{f_{\rm E}} = 0.11$; for the S0 galaxy fraction, we obtain $\sigma_{f_{\rm S0}} = 0.05$; and for the late-type galaxy fraction (Sp+Irr), we obtain $\sigma_{f_{\rm Sp+Irr}} = 0.11$. The uncertainty in the early-type galaxy fraction (E+S0) is $\sigma_{f_{\rm E+S0}} = 0.11$. These uncertainties are comparable in size to those obtained by Postman et al. (2005).

Note that in this study we have not taken into account the potential impact of surface brightness dimming, the effect of which can impair the ability to distinguish between, e.g., ellipticals/S0s and S0/Sa galaxies. Postman et al. (2005) conducted simulations in order to quantify the size of this effect in their ACS study of the morphology–density relation in $z \sim 1$ clusters, and found that the effect of surface brightness dimming was successfully mitigated by their chosen exposure times (typically ≈12,000 s in z_{850}). We therefore expect that the impact of surface brightness dimming on our results is alleviated to some extent by our long exposure time, ≈40% longer than the typical exposure time used by Postman et al. (2005), and by the broad morphological bins we have adopted.

3.3. Photometric Redshifts

Secure spectroscopic redshifts have been obtained for a total of 58 galaxies within the 3.′04 field covered by the ACS and MOIRCS observations. The majority of these redshifts come from observations of J2215.9−1738 using the DEep Imaging Multi-Object Spectrograph (DEIMOS; Faber et al. 2003) on the 10 m Keck II telescope, and the Focal Reducer and Low Dispersion Spectrograph (FORS2; Appenzeller et al. 1998) on the 8 m Very Large Telescope (VLT), and are described in Hilton et al. (2007). Observations through a further three DEIMOS slit masks have been obtained subsequent to this work; one being observed in 2007 September, and two in 2008

September. Details of the 2007 and 2008 Keck observations will be presented in S. A. Stanford et al. (2009, in preparation). Of the 58 galaxies with spectroscopic redshifts, 24 are cluster members, and so we chose to use the available four-band (i_{775}, z_{850}, J, K_s) photometry to determine cluster membership using photometric redshifts, for all galaxies in the K_s-selected catalog described in Section 3.1.

We used the spectral template fitting code EAZY (Brammer et al. 2008) to estimate photometric redshifts. EAZY has been designed to be especially useful in cases where spectroscopic redshifts are only available for a biased subset of galaxies. This is the case for our data set, as color, magnitude criteria were used to preferentially select likely cluster members as spectroscopic targets. Furthermore, the limited size of our spectroscopic subsample makes the use of "training set"-type techniques inappropriate, such as, e.g., neural-network based redshift estimates (Collister & Lahav 2004), or iterative correction of empirical spectral templates (Feldmann et al. 2006). We used the default set of five spectral templates included with EAZY, which is constructed by applying the non-negative matrix factorization technique of Blanton & Roweis (2007) to a set of 3000 stellar population models from the PEGASE library (Fioc & Rocca-Volmerange 1997), and a catalog of synthetic galaxy photometry derived from the semianalytic simulation of De Lucia & Blaizot (2007). We chose to use the option within EAZY to fit a linear combination of all of the templates to our galaxy catalog, over a redshift range of $0 < z < 4$, using the 1.″0 aperture magnitudes as the input photometry. Finally, we chose to use the K-magnitude based Bayesian redshift prior included with EAZY, which is derived from the synthetic, semianalytic model galaxy photometry used to define the template set, and adopted the maximum likelihood redshift estimate after the application of this prior as the redshift estimate z_p for each galaxy.

We checked the accuracy of the photometric redshift estimates produced by EAZY by comparison with the spectroscopic subsample. Given the wavelength coverage of our available photometric bands, we would not expect to obtain reliable photometric redshifts for galaxies with redshifts below $z < 1$, as photometric redshift techniques rely on identifying strong spectral breaks in order to assign redshift estimates, and the i_{775}-band only drops below 4000 Å in the rest frame at $z \gtrsim 1$. We therefore performed the check on the photometric redshift accuracy on the 36 galaxies with spectroscopic redshifts $z_s > 1$. We found that the typical scatter σ_{δ_z} in the photometric redshift residuals $\delta z = (z_s - z_p)/(1 + z_s)$ was $\sigma_{\delta_z} = 0.039$, where σ_{δ_z} was estimated using a biweight scale estimator (e.g., Beers et al. 1990), which is robust to outliers. The photometric redshifts appear to be almost unbiased in this redshift range, as the median $\delta z = +0.015$; however, a small number of objects have overestimated photometric redshifts, as can be seen from the negative tail of the distribution shown in Figure 3.

A cut of $| z_p - z_c | < 2 \times \sigma_{\delta z}(1 + z_c)$ was used to define cluster membership, where z_c is the cluster redshift of $z = 1.46$—i.e., galaxies with $1.27 < z_p < 1.65$ were considered to be members of the cluster. We used the spectroscopic subsample to assess the amount of contamination from galaxies with spurious photometric redshifts (i.e., with $z_s < 1.27$, $z_s > 1.65$); contamination from interlopers, defined as galaxies with velocities outside of the range $\pm 3\sigma_v$ around the cluster redshift, where σ_v is the line of sight velocity dispersion measured in Hilton et al. (2007; i.e., $z_s > 1.46 + 0.015$ or $z_s < 1.46$–0.015, but $1.27 < z_s < 1.65$); and missing spectroscopically identified members (i.e., with $z_p < 1.27$, $z_p > 1.65$ and $1.445 < z_s < 1.475$).

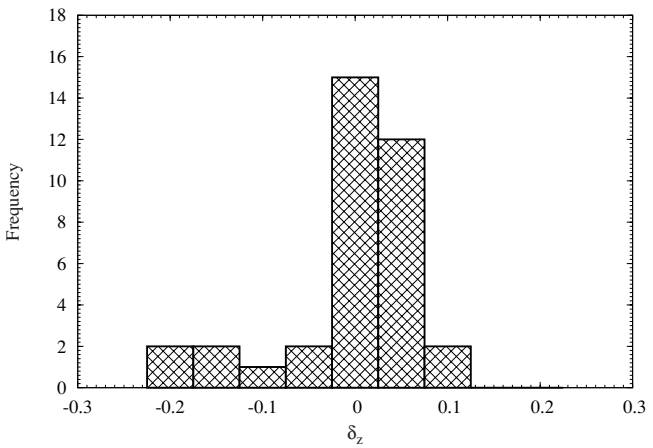

Figure 3. Histogram of the photometric redshift residuals $\delta z = (z_s - z_p)/(1+z_s)$, where z_s is the spectroscopic redshift, and z_p is the corresponding photometric redshift. All galaxies with spectroscopic redshifts $z_s > 1$ are included. The photometric redshifts are almost unbiased; the median of the distribution is $\delta z = +0.015$.

Initially, using only the cut in z_p to define membership, a total of 13 galaxies (22% of the spectroscopic subsample) were identified as having spurious photometric redshifts, all with $z_s < 1$. However, galaxies with unreliable photometric redshift estimates have flat or multimodal posterior redshift probability distributions, and can be easily identified by their p_{Δ_z} value (introduced by Benítez 2000, and labeled ODDS in the output from EAZY), which is the fraction of the integrated probability that lies within $\pm\Delta z$ of the photometric redshift estimate z_p (in the case of EAZY, $\Delta_z = 0.2$). Galaxies with lower p_{Δ_z} values have broader redshift probability distributions, and correspondingly less reliable photometric redshift estimates. Applying a cut of $p_{\Delta_z} > 0.9$ reduces the number of spurious photometric redshifts in the spectroscopic subsample to two galaxies (3.4% of the spectroscopic subsample). We therefore chose to use this cut in p_{Δ_z} in all that follows. A more conservative cut of $p_{\Delta_z} > 0.95$ reduces the number of galaxies with spurious photometric redshifts to just a single galaxy, but this comes at the cost of a smaller sample size and increased error bars on the derived CMR parameters (see Section 4.3).

The number of spectroscopically confirmed noncluster members contaminating the photometrically selected sample was found to be three (10.3% of the sample). However, four spectroscopically confirmed cluster members were missed by the photometric redshift selection (16.7% of the sample of 24 confirmed cluster members). Using a broader cut in z_p than we have applied naturally reduces the fraction of missed spectroscopic members, but at the cost of significantly increasing the contamination from spectroscopically confirmed interlopers. We show in Sections 4.1 and 4.3 that our measurements are robust to reasonable changes of the parameters governing the photometric redshift selection.

We further refined our photometric membership selection by excluding from the sample all galaxies with K_s-band magnitudes brighter than the BCG, i.e., $K_s < 20.57$. Although J2215.9−1738 lacks an obvious BCG, it possesses several candidates that are of similar brightness (see Collins et al. 2009), and this additional cut helps by removing seven bright, blue ($z_{850} - J < 1.0$), lower-redshift galaxies from the sample. These objects are probably at $z \approx 1.3$, as indicated from their photometric redshifts, and one of these objects is a known interloper with spectroscopic redshift $z_s = 1.301$. Finally, we removed

from the sample all known interlopers with spectroscopic redshifts, and added back in the four spectroscopically confirmed members missed by the photometric redshift selection.

The final sample of photometrically selected members within the ACS/MOIRCS imaging area contains 64 galaxies. The colors, magnitudes, spectroscopic and photometric redshifts, and morphologies of the sample are recorded in Table 1.

4. RESULTS

4.1. Morphologies

Figure 4 shows postage stamp images of all the galaxies with morphological classifications (i.e., all galaxies with $z_{850} \leqslant 24$), located within 0.75 Mpc of the cluster X-ray position, and selected as cluster members using the photometric criteria described in Section 3.3. In addition to the z_{850}-band data from which the morphology of each object was determined, we also show a corresponding postage stamp taken from the K_s-band image that was used to perform the object detection (see Section 3.1). Only four objects in this sample were found to be blended in the K_s-selected catalog—these are IDs 824, 610, 696, and 1047, and are noted with a pair of morphologies in Figure 4 and Table 1.

Within a radius of 0.5 Mpc of the cluster X-ray position, there are a total of 39 galaxies with morphological classifications. The fraction of elliptical galaxies in this subsample is $f_{\rm E} = 0.54 \pm 0.17$; the fraction of lenticular galaxies is $f_{\rm S0} = 0.08 \pm 0.07$; and the fraction of late-type galaxies is $f_{\rm Sp+Irr} = 0.38 \pm 0.15$. The combined fraction of early-type galaxies is $f_{\rm E+S0} = 0.62 \pm 0.17$.

In calculating the errors on the morphological fractions quoted above, we add in quadrature the classification error (see Section 3.2), the Poisson uncertainty, and the uncertainty in cluster membership due to the photometric redshift selection. To account for this latter effect, we perform 1000 Monte Carlo simulations in which the photometric redshift of every galaxy is replaced by a random variate drawn from its photometric redshift probability distribution, as output by EAZY, and apply the algorithm described in Section 3.3 to select cluster members. We find that the dominant source of error is the classification error; the photometric redshift selection increases the size of the uncertainties by at most ≈4% for a given morphological bin.

To further check that the results are robust to the choice of parameters used to define the photometric redshift selection, we also calculated the morphological fractions for different photometric redshift cuts. For a more conservative choice of $p_{\Delta_z} > 0.95$, we obtain consistent results of $f_{\rm E} = 0.56 \pm 0.17$; $f_{\rm S0} = 0.06 \pm 0.07$; and $f_{\rm Sp+Irr} = 0.38 \pm 0.16$, for a sample of 34 galaxies within a radius of 0.5 Mpc. Similarly, for a more stringent photometric redshift cut of $1.36 < z_p < 1.56$ with $p_{\Delta_z} > 0.9$, we obtain $f_{\rm E} = 0.55 \pm 0.18$; $f_{\rm S0} = 0.06 \pm 0.07$; and $f_{\rm Sp+Irr} = 0.39 \pm 0.16$, for a sample of 31 galaxies within the same selection radius. Considering only the 19 galaxies with spectroscopic redshifts located within 0.5 Mpc of the cluster X-ray position, we obtain results consistent with those above, although with larger uncertainties. For this sample, we find $f_{\rm E} = 0.58 \pm 0.21$; $f_{\rm S0} = 0.05 \pm 0.07$; and $f_{\rm Sp+Irr} = 0.37 \pm 0.18$.

Given the large uncertainties, we are unable to examine the variation of the morphological fraction with radius. For example, extending the radius within which the morphological fractions are calculated to 0.75 Mpc does not change our results, as it only increases the sample size by a further three galaxies.

The object identified as the BCG in J2215.9−1738, ID 688, has a clear S0 morphology as seen in Figure 4. It is the brightest cluster member in the K_s band (although there are in fact several other candidates of similar brightness), and has a spectrum consistent with a luminous red galaxy (LRG) template (see Figure 1 of Hilton et al. 2007). However, it lies ≈300 kpc away from the cluster X-ray position. Although this would be unusual for clusters at low redshift, we note that the two brightest members of the $z = 1.10$ cluster RDCS J0910+5422 also have S0 morphologies, and furthermore, are located at cluster-centric distances >300 kpc (Mei et al. 2006a). Therefore, it is possible that J2215.9−1738 is not untypical of clusters at this epoch in this regard, given the small number of objects currently known at $z > 1$. A comparison of the stellar masses of BCGs in a sample of $z > 1$ clusters, including J2215.9−1738, with the latest semianalytic models of galaxy formation is presented in Collins et al. (2009).

4.2. Color–Magnitude Diagrams

We present the z_{850}–J and z_{850}–K_s CMDs with fitted CMRs (Section 4.3) in Figures 5 and 6, respectively. Panel (a) of each figure shows all galaxies in the combined ACS/MOIRCS imaging area; panel (b) shows only members selected according to the photometric criteria described in Section 3.3. In each of these plots, we show the approximate 5σ limiting magnitude for galaxies as a blue vertical dashed line (estimated from the size of the photometric errors); the corresponding 5σ limit in color as a diagonal dashed blue line; and the approximate limit of the morphological classification caused by the $z_{850} < 24$ limit (see Section 3.2) as a diagonal dashed green line.

Along the top axis of each plot, we show the magnitude relative to the expected characteristic magnitude (M^*; labeled as J^* or K_s^* appropriately for each band in the plots) of the galaxy luminosity function at $z = 1.46$. The value of M^* was estimated by passively evolving the value of K^* found for clusters at $z = 0.9$ by De Propris et al. (1999) to $z = 1.46$, transformed to the passbands used in this paper. The evolution correction was performed by adopting a Bruzual & Charlot (2003) single burst of star formation model, beginning at redshift $z_f = 3$, decaying exponentially with characteristic timescale $\tau = 0.1$ Gyr, with solar metallicity, and Salpeter (1955) initial mass function (IMF). This model acceptably reproduces the observed evolution of K^* over the redshift range $0.1 < z < 0.9$ for the data in De Propris et al. (1999).

It is immediately apparent from Figures 5 and 6 that the bright end of the CMR in J2215.9−1738 is unpopulated: the brightest galaxies have $K_s \approx 20.6$, approximately as bright as the expected value of M^*. In contrast, the only other $z > 1.3$ X-ray selected cluster currently known, XMMU J2235.3−2557 at $z = 1.39$, has four spectroscopically confirmed members with K_s magnitudes in the range $18.9 < K_s({\rm AB}) < 20.6$, within a 0.2 Mpc radius of the cluster center (Lidman et al. 2008). This corresponds to a difference in absolute magnitude of ∼1.5 mag between the BCGs (see also Collins et al. 2009), neglecting the correction for passive evolution, as the difference in lookback time between the two clusters is only 0.2 Gyr.

Given the small number of systems observed to date at such high redshifts, it is unclear which of these objects is more typical of the general cluster population at this epoch. We note that the brightest galaxies in the compact cluster associated with the $z = 1.51$ galaxy GDDS-12-5859 have similar K-band magnitudes to the brightest members of J2215.9−1738 (McCarthy et al. 2007). However, further spectroscopic observations of this object are required to confirm its nature as a gravitationally bound system at $z = 1.5$.

Table 1
Photometrically Selected Members of J2215.9−1738

ID	R.A. (J2000)	Decl. (J2000)	$z_{850}-J$	$z_{850}-K_s$	J	K_s	z_s	z_p	Mph.[a]	H07[b]	r (kpc)[c]
742	22 15 58.464	−17 37 58.58	1.450 ± 0.034	2.356 ± 0.030	21.780 ± 0.028	20.901 ± 0.019	1.452	$1.47^{+0.55}_{-0.18}$	E	1	33
803	22 15 58.368	−17 38 06.46	1.478 ± 0.046	2.489 ± 0.042	22.296 ± 0.040	21.246 ± 0.024	···	$1.41^{+0.66}_{-0.14}$	E	···	37
748	22 15 58.872	−17 37 59.26	1.314 ± 0.038	2.243 ± 0.032	21.817 ± 0.033	21.050 ± 0.024	1.451	$1.37^{+0.66}_{-0.18}$	E	2	53
789	22 15 58.056	−17 38 04.59	0.623 ± 0.139	1.144 ± 0.136	24.372 ± 0.198	23.597 ± 0.145	1.465	$1.32^{+0.80}_{-0.93}$	···	···	57
770	22 15 59.040	−17 38 02.54	1.478 ± 0.042	2.576 ± 0.036	21.773 ± 0.033	20.858 ± 0.022	1.454	$1.42^{+0.71}_{-0.14}$	E	3	65
*824	22 15 58.488	−17 38 10.53	1.298 ± 0.033	2.366 ± 0.028	21.484 ± 0.028	20.575 ± 0.019	1.465	$1.37^{+0.75}_{-0.17}$	Irr, E	4	68
821	22 15 58.848	−17 38 09.85	1.117 ± 0.046	1.715 ± 0.043	22.368 ± 0.050	21.773 ± 0.044	1.453	$1.43^{+0.56}_{-0.14}$	E	7	75
713	22 15 58.392	−17 37 53.68	1.373 ± 0.045	2.323 ± 0.039	22.289 ± 0.043	21.317 ± 0.027	···	$1.35^{+0.68}_{-0.15}$	E	···	76
771	22 15 57.864	−17 38 02.11	1.291 ± 0.120	2.072 ± 0.104	23.485 ± 0.117	22.740 ± 0.085	···	$1.44^{+0.68}_{-0.32}$	···	···	77
745	22 15 59.088	−17 37 58.54	1.212 ± 0.109	1.853 ± 0.099	23.678 ± 0.089	22.970 ± 0.067	···	$1.47^{+0.62}_{-0.31}$	···	···	79
712	22 15 59.136	−17 37 54.22	1.569 ± 0.049	2.666 ± 0.046	21.737 ± 0.029	20.724 ± 0.017	1.462	$1.79^{+0.34}_{-0.46}$	E	8	104
823	22 15 59.376	−17 38 09.88	0.630 ± 0.144	0.971 ± 0.140	23.938 ± 0.110	23.891 ± 0.142	1.467	$1.44^{+0.80}_{-1.12}$	···	···	123
792	22 15 59.544	−17 38 05.24	1.308 ± 0.063	2.245 ± 0.059	22.190 ± 0.045	21.283 ± 0.031	···	$1.38^{+0.74}_{-0.20}$	Sp	···	128
754	22 15 57.432	−17 37 57.90	0.141 ± 0.371	1.529 ± 0.197	24.109 ± 0.258	23.052 ± 0.136	1.454	$1.16^{+2.70}_{-0.65}$	···	9	135
683	22 15 57.864	−17 37 48.61	1.221 ± 0.124	1.926 ± 0.111	23.318 ± 0.119	22.742 ± 0.102	···	$1.48^{+0.66}_{-0.40}$	···	···	140
875	22 15 58.008	−17 38 18.13	1.508 ± 0.064	2.640 ± 0.055	22.237 ± 0.047	21.308 ± 0.029	···	$1.36^{+0.78}_{-0.09}$	Sp	···	145
747	22 15 59.688	−17 37 59.70	1.368 ± 0.081	2.702 ± 0.069	21.982 ± 0.049	21.044 ± 0.031	···	$1.50^{+0.81}_{-0.22}$	Irr	···	146
878	22 15 57.864	−17 38 18.70	1.098 ± 0.078	1.693 ± 0.073	23.246 ± 0.072	22.648 ± 0.067	···	$1.33^{+0.59}_{-0.32}$	···	···	157
749	22 15 59.832	−17 38 00.45	1.166 ± 0.064	1.968 ± 0.057	22.601 ± 0.058	22.039 ± 0.052	···	$1.45^{+0.68}_{-0.25}$	E	···	162
810	22 15 57.192	−17 38 07.80	0.552 ± 0.046	1.131 ± 0.041	22.386 ± 0.043	22.051 ± 0.045	1.450	$1.36^{+0.67}_{-1.05}$	Irr	11	164
759	22 15 59.880	−17 37 59.26	1.284 ± 0.034	2.028 ± 0.032	22.029 ± 0.034	21.379 ± 0.029	···	$1.40^{+0.53}_{-0.17}$	E	···	169
899	22 15 58.224	−17 38 22.12	1.036 ± 0.056	2.385 ± 0.044	22.551 ± 0.068	21.349 ± 0.034	···	$1.46^{+0.99}_{-0.32}$	Sp	···	169
708	22 15 57.240	−17 37 53.22	0.854 ± 0.073	2.166 ± 0.050	22.385 ± 0.062	21.414 ± 0.038	1.454	$1.30^{+0.92}_{-0.48}$	Sp	13	171
653	22 15 57.720	−17 37 45.55	1.406 ± 0.059	2.673 ± 0.049	21.873 ± 0.041	20.911 ± 0.025	···	$1.33^{+0.88}_{-0.10}$	Irr	···	172
786	22 15 56.928	−17 38 04.70	0.748 ± 0.055	1.326 ± 0.051	22.210 ± 0.044	21.815 ± 0.046	1.445	$1.43^{+0.77}_{-1.17}$	Irr	···	191
629	22 15 58.344	−17 37 37.30	0.722 ± 0.095	1.218 ± 0.092	23.266 ± 0.112	22.707 ± 0.100	1.453	$1.44^{+0.76}_{-1.15}$	Sp	14	214
614	22 15 59.064	−17 37 37.95	1.207 ± 0.058	2.095 ± 0.052	22.358 ± 0.055	21.557 ± 0.040	···	$1.45^{+0.69}_{-0.23}$	E	···	218
715	22 15 56.712	−17 37 53.07	1.256 ± 0.066	2.106 ± 0.058	22.882 ± 0.052	22.116 ± 0.039	···	$1.34^{+0.66}_{-0.22}$	···	···	230
853	22 16 00.216	−17 38 15.43	1.248 ± 0.105	2.171 ± 0.090	23.359 ± 0.093	22.582 ± 0.068	···	$1.40^{+0.77}_{-0.30}$	···	···	235
692	22 16 00.384	−17 37 50.59	1.235 ± 0.038	2.194 ± 0.032	21.765 ± 0.033	20.990 ± 0.024	1.451	$1.33^{+0.69}_{-0.19}$	E	···	249
*696	22 16 00.648	−17 37 51.67	1.533 ± 0.054	2.553 ± 0.047	22.186 ± 0.046	21.166 ± 0.027	1.471	$1.95^{+0.12}_{-0.65}$	E, E	15	275
643	22 16 00.384	−17 37 42.74	0.739 ± 0.045	1.599 ± 0.037	22.741 ± 0.055	21.755 ± 0.034	···	$1.31^{+0.11}_{-0.64}$	Irr	···	282
688	22 15 56.184	−17 37 49.90	1.367 ± 0.023	2.282 ± 0.020	21.482 ± 0.021	20.568 ± 0.014	1.454	$1.37^{+0.64}_{-0.15}$	S0	16	300
723	22 15 56.016	−17 37 55.05	0.292 ± 0.145	0.554 ± 0.158	24.117 ± 0.160	23.876 ± 0.189	1.460	$1.49^{+2.11}_{-1.14}$	···	···	307
591	22 16 00.096	−17 37 33.92	0.715 ± 0.109	0.839 ± 0.132	23.200 ± 0.116	22.858 ± 0.128	1.454	$1.46^{+0.56}_{-1.14}$	···	···	309
1018	22 15 59.472	−17 38 37.39	0.470 ± 0.051	0.229 ± 0.089	22.396 ± 0.049	22.765 ± 0.101	1.457	$1.57^{+0.33}_{-1.48}$	Sp	18	318
872	22 16 00.936	−17 38 18.20	1.404 ± 0.043	2.290 ± 0.039	22.267 ± 0.035	21.379 ± 0.024	···	$1.48^{+0.56}_{-0.19}$	E	···	323
888	22 15 56.040	−17 38 20.61	1.350 ± 0.048	2.326 ± 0.040	22.383 ± 0.054	21.321 ± 0.031	···	$1.36^{+0.70}_{-0.17}$	S0	···	335
*610	22 15 56.304	−17 37 37.99	1.362 ± 0.033	2.350 ± 0.029	21.545 ± 0.030	20.695 ± 0.022	···	$1.27^{+0.75}_{-0.09}$	E, E	···	337
982	22 16 00.408	−17 38 32.42	1.232 ± 0.111	1.757 ± 0.109	23.159 ± 0.089	22.887 ± 0.106	···	$1.36^{+0.60}_{-0.22}$	···	···	342
1004	22 16 00.576	−17 38 36.42	1.314 ± 0.046	2.178 ± 0.042	22.049 ± 0.041	21.218 ± 0.029	···	$1.38^{+0.63}_{-0.19}$	E	···	381
*1047	22 16 00.096	−17 38 42.61	0.946 ± 0.076	1.777 ± 0.065	23.009 ± 0.067	22.253 ± 0.050	1.463	$1.45^{+0.85}_{-1.06}$	Sp, E	···	390
798	22 15 55.200	−17 38 04.16	0.978 ± 0.059	2.079 ± 0.047	22.366 ± 0.063	21.457 ± 0.042	···	$1.27^{+0.15}_{-0.34}$	Irr	···	399
529	22 15 56.808	−17 37 21.90	1.310 ± 0.097	2.432 ± 0.080	22.578 ± 0.089	21.538 ± 0.051	···	$1.55^{+0.72}_{-0.31}$	Irr	···	400
500	22 15 59.808	−17 37 17.54	0.722 ± 0.042	1.623 ± 0.031	22.415 ± 0.044	21.602 ± 0.030	···	$1.27^{+0.10}_{-0.50}$	E	···	412
526	22 15 56.544	−17 37 21.36	0.613 ± 0.033	1.479 ± 0.026	22.361 ± 0.039	21.489 ± 0.025	1.446	$1.30^{+0.13}_{-0.88}$	E	···	421
939	22 16 01.896	−17 38 27.09	0.451 ± 0.065	0.415 ± 0.086	23.029 ± 0.077	22.866 ± 0.094	···	$1.59^{+0.49}_{-1.29}$	S0	···	460
538	22 15 55.200	−17 37 22.36	1.602 ± 0.045	2.476 ± 0.041	22.119 ± 0.034	21.362 ± 0.027	1.460	$1.82^{+0.15}_{-0.38}$	S0	···	524
697	22 16 03.432	−17 37 51.24	0.737 ± 0.131	1.357 ± 0.116	23.992 ± 0.227	22.817 ± 0.114	1.462	$1.36^{+0.86}_{-0.99}$	···	···	604
303	22 15 56.976	−17 36 54.18	1.449 ± 0.221	2.322 ± 0.196	24.164 ± 0.188	23.143 ± 0.106	···	$1.54^{+0.69}_{-0.47}$	···	···	606
957	22 16 03.144	−17 38 29.83	1.350 ± 0.032	2.335 ± 0.029	21.451 ± 0.027	20.628 ± 0.019	···	$1.39^{+0.68}_{-0.17}$	E	···	607
1080	22 15 54.288	−17 38 48.22	1.581 ± 0.134	2.114 ± 0.128	23.007 ± 0.085	22.776 ± 0.098	···	$1.63^{+0.33}_{-0.28}$	···	···	639
1118	22 15 54.624	−17 38 55.06	1.376 ± 0.093	2.860 ± 0.071	22.864 ± 0.083	21.326 ± 0.030	···	$1.39^{+0.91}_{-0.11}$	···	···	646
1243	22 15 59.808	−17 39 18.21	1.258 ± 0.105	2.101 ± 0.091	23.069 ± 0.073	22.226 ± 0.050	···	$1.48^{+0.69}_{-0.33}$	···	···	660

Table 1
(Continued)

ID	R.A. (J2000)	Decl. (J2000)	z_{850}–J	z_{850}–K_s	J	K_s	z_s	z_p	Mph.[a]	H07[b]	r (kpc)[c]
1028	22 16 03.720	−17 38 38.68	1.485 ± 0.136	2.508 ± 0.120	23.366 ± 0.109	22.505 ± 0.072	···	$1.44^{+0.72}_{-0.24}$	···	···	701
1149	22 15 54.000	−17 39 01.65	1.026 ± 0.064	1.873 ± 0.052	22.087 ± 0.071	21.289 ± 0.050	···	$1.55^{+0.73}_{-1.02}$	E	···	739
96	22 15 56.160	−17 36 37.80	0.429 ± 0.097	1.102 ± 0.079	23.290 ± 0.088	23.025 ± 0.100	1.455	$1.35^{+1.06}_{-1.01}$	E	···	770
450	22 16 03.816	−17 37 10.38	1.062 ± 0.094	1.074 ± 0.118	23.643 ± 0.147	23.014 ± 0.123	···	$1.65^{+0.32}_{-0.24}$	···	···	779
9	22 16 00.839	−17 39 31.96	1.392 ± 0.107	2.906 ± 0.089	23.226 ± 0.080	21.841 ± 0.032	···	$1.48^{+0.94}_{-0.14}$	···	···	808
1201	22 16 03.168	−17 39 11.05	0.736 ± 0.059	1.488 ± 0.051	22.347 ± 0.065	21.770 ± 0.058	···	$1.29^{+0.12}_{-0.57}$	Irr	···	809
858	22 16 05.376	−17 38 16.44	1.036 ± 0.069	1.842 ± 0.056	22.518 ± 0.055	22.000 ± 0.050	···	$1.34^{+0.72}_{-0.42}$	Sp	···	840
850	22 16 05.448	−17 38 14.85	1.075 ± 0.112	1.710 ± 0.104	23.331 ± 0.098	22.897 ± 0.101	···	$1.52^{+0.69}_{-0.80}$	···	···	846
8	22 16 01.776	−17 39 32.04	0.938 ± 0.037	1.321 ± 0.037	21.997 ± 0.025	21.661 ± 0.026	···	$1.50^{+0.48}_{-0.15}$	···	···	855
539	22 16 05.592	−17 37 22.51	0.957 ± 0.085	1.476 ± 0.081	23.441 ± 0.079	22.831 ± 0.070	···	$1.62^{+0.57}_{-1.11}$	···	···	922

Notes. Sorted in order of radial distance from the cluster X-ray position. Units of right ascension are hours, minutes, and seconds, and units of declination are degrees, minutes, and seconds. Colors are measured through 1.″0 diameter apertures. J and K_s total magnitudes are measured using SEXTRACTOR MAG_AUTO. All magnitudes are on the AB system. Objects IDs marked with an asterisk (*) are blended in the K_s-selected catalog, and so their photometry may not be reliable. Uncertainties quoted on photometric redshifts z_p are 95% confidence intervals; all photometric redshifts have $p_{\Delta_z} > 0.9$ (see Section 3.3).

[a] Morphology: E=elliptical, S0=lenticular, Sp=spiral, Irr=irregular (see Section 3.2). Only objects brighter than $z_{850} \leqslant 24$ were morphologically classified. Objects assigned multiple morphologies are blended in the K_s-selected catalog; the morphology of the easternmost component (see Figure 4) is given first.

[b] Object ID in Table 2 of Hilton et al. (2007).

[c] Radial distance from the cluster X-ray position.

Inspection of Figures 5 and 6 shows that limiting the CMR fitting to a purely morphologically selected sample of E+S0 galaxies would restrict the total magnitude range in comparison to the magnitude limit of the complete sample. We therefore chose to perform the analysis on two samples—a morphologically selected sample of E+S0 galaxies (hereafter referred to as the "morphologically selected sample"), and a sample defined without this restriction, spanning a larger magnitude range (hereafter referred to as the "photometrically selected sample"). In both cases, we only include galaxies that pass the photometric membership selection criteria described in Section 3.3, to reduce the contamination from noncluster member galaxies significantly. For the photometrically selected sample, we applied an additional color cut of $0.8 < z_{850} - J < 1.6$, $1.5 < z_{850}$–$K_s < 3.0$ as appropriate for the CMR being fitted, in order to avoid biasing the fits by the inclusion of a handful of faint galaxies much bluer than the red sequence.

An additional benefit of performing the analysis on a sample not selected on the basis of morphology is to examine the sensitivity of the results to the morphological classification. Systematic misclassification of some galaxies, for example, face-on S0s as ellipticals, or flattened late-type galaxies as S0s, would increase the apparent scatter about the CMR and result in the inference of younger galaxy ages (see, e.g., Mei et al. 2009).

4.3. Color–Magnitude Relations

The CMRs were fitted to the color–magnitude data for each sample, defined in Section 4.2, using a robust biweight linear least squares method. We estimated the errors on the fits in a Monte Carlo fashion: we generated 1000 realizations of the data, replacing the color of each galaxy with a random variate, assuming that the color errors have a Gaussian distribution, and fitted the CMR for each of these simulated data sets. The 1σ errors in the slope and intercept of the measured CMR were taken to be the standard deviations of the slopes and intercepts measured for the 1000 simulated data sets.

For the morphologically selected sample of early-type (E+S0) galaxies, we obtained the following relations:

$$z_{850} - J = (-0.049 \pm 0.062) \quad (J - 22.5) + (1.335 \pm 0.046), \tag{1}$$

$$z_{850} - K_s = (-0.221 \pm 0.057) \quad (K_s - 22.5) + (2.012 \pm 0.091). \tag{2}$$

For the photometrically selected sample, we obtained similar results:

$$z_{850} - J = (-0.112 \pm 0.026) \quad (J - 22.5) + (1.282 \pm 0.016), \tag{3}$$

$$z_{850} - K_s = (-0.299 \pm 0.021) \quad (K_s - 22.5) + (1.914 \pm 0.028). \tag{4}$$

Both the slopes and intercepts measured for the morphologically and photometrically selected samples agree at better than $< 2\sigma$ for both the fits to the z_{850}–J and z_{850}–K_s CMRs, with the agreement being slightly better between the two samples in z_{850}–J. The uncertainties on the CMR slopes and intercepts are relatively large, due to the large scatter about the CMRs that can be seen in Figures 5 and 6.

As Figures 5 and 6 show, there are only 10 spectroscopically confirmed members with early-type morphologies located within 0.5 Mpc of the cluster X-ray position with $J < 22.5$. We found that fitting the CMR for this purely spectroscopically selected sample gave significantly worse constraints on the CMR than the samples supplemented with photometric redshifts; for example, the slope of the z_{850}–J CMR is found to be -0.262 ± 0.127. This is driven by one object (ID 526), which has a clear elliptical morphology (see Figure 4), but is significantly bluer than the other spectroscopically selected early-type

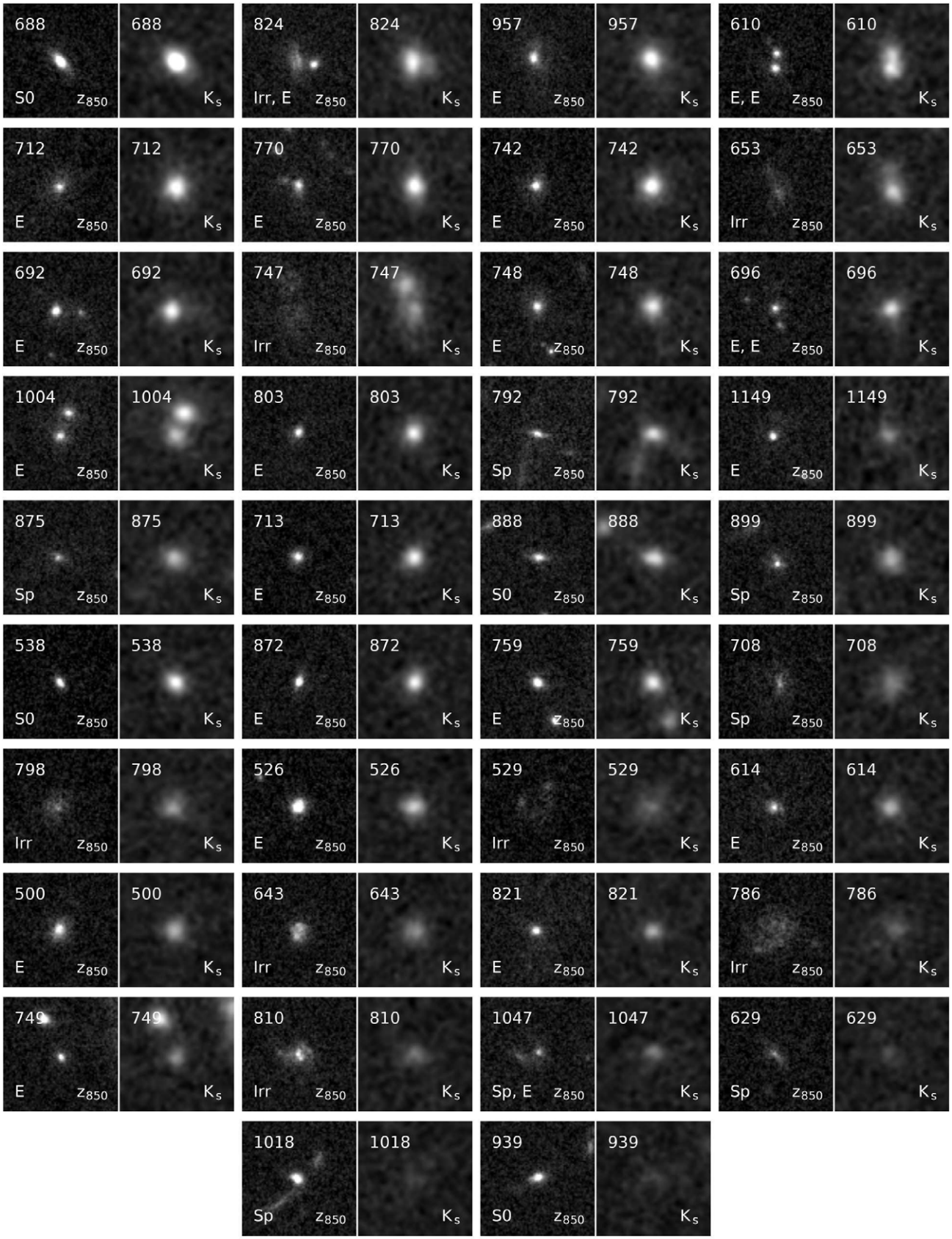

Figure 4. Postage stamp images of all photometrically selected members of J2215.9−1738 for which morphological classification was carried out, located within a radius of 0.75 Mpc of the cluster X-ray position, and ordered by K_s magnitude, from brightest (top left) to faintest (bottom right). The left postage stamp of each pair is taken from the ACS z_{850}-band image; the right-hand image of each pair is taken from the MOIRCS K_s-band data which was used to perform the object detection (see Section 3.1). Each postage stamp is 3.″75 on a side, with east at the left. The number in the top left-hand corner of each plot is the galaxy ID number in Table 1; the galaxy morphology is indicated in the bottom left-hand corner of each ACS z_{850} image. Note that a few objects (IDs 824, 610, 696, and 1047) are blended in the K_s-selected catalog; these are assigned multiple morphologies, with the morphology of the easternmost component being quoted first.

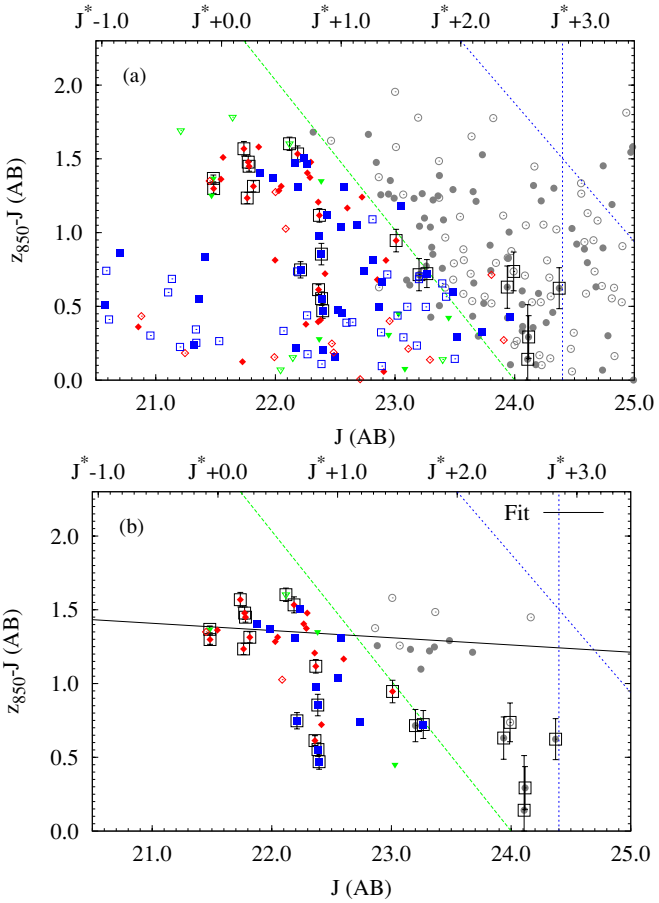

Figure 5. z_{850}–J vs. J color–magnitude diagram for J2215.9−1738 for (*a*) all galaxies; and (*b*) photometrically selected members only (see Section 3.3). Elliptical galaxies are marked as red circles; S0s with green triangles; late-type galaxies with blue squares; and galaxies for which morphologies were not determined with gray circles. Filled symbols are located within radius $r < 0.5$ Mpc of the cluster X-ray position; open symbols are located at $r > 0.5$ Mpc. Symbols enclosed within a black box are cluster members with secure spectroscopic redshifts; these points are marked with error bars, indicating the typical size of the color error in a particular region of the CMD. The approximate 5σ limiting magnitude for galaxies is shown by the vertical dashed blue line; the corresponding 5σ limit in z_{850}–J color is shown by the diagonal dashed blue line; the diagonal dashed green line marks the approximate limit of the morphological selection. The solid black line shows the fit to the CMR for morphologically selected E+S0 galaxies (see Table 2).

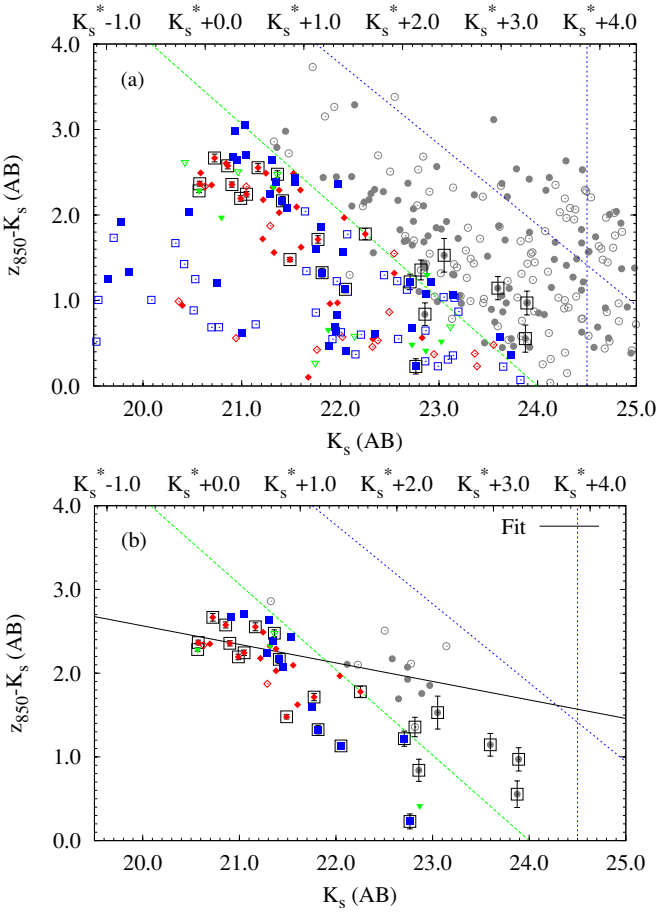

Figure 6. z_{850}–K_s vs. K_s CMD for J2215.9−1738 for (*a*) all galaxies; and (*b*) photometrically selected members only (see Section 3.3). The symbols and lines have the same meaning as in Figure 6. The solid black line shows the fit to the CMR for morphologically selected E+S0 galaxies (see Table 2).

galaxies. For this reason, we do not consider the purely spectroscopically selected galaxy sample further in this paper.

The observed scatter about the CMR was measured using a biweight scale estimate of the color residuals, with the error being estimated from 1000 bootstrap samples. The intrinsic scatter $\sigma_{\rm int}$ in the CMR was estimated by subtracting in quadrature the rms of the color errors of the galaxy sample to which the CMR was fitted. For the morphologically selected sample of early-type (E+S0) galaxies, we measured $\sigma_{\rm int}(z_{850}{-}J) = 0.123 \pm 0.049$, and $\sigma_{\rm int}(z_{850}{-}K_s) = 0.173 \pm 0.052$. For the photometrically selected sample, we found $\sigma_{\rm int}(z_{850}{-}J) = 0.118 \pm 0.034$, and $\sigma_{\rm int}(z_{850}{-}K_s) = 0.237 \pm 0.037$. The measurements of intrinsic scatter are therefore in excellent agreement, at better than $< 1\sigma$, between the morphologically and photometrically selected samples. This suggests that systematic morphological classification errors of the type described in Section 4.2 are not a problem at the level of precision achievable with our galaxy sample.

We examined the dependence of our results on the photometric redshift selection in a number of ways. Adopting a conservative cut of $p_{\Delta_z} > 0.95$, we found no significant differences with the results reported above: the differences between the CMR slope and intercept values in each band and for each sample are significant at the $< 2\sigma$ level. Restricting the photometric redshift selection to only galaxies with $z_p = 1.46 \pm 0.1$, with $p_{\Delta_z} > 0.9$, we find likewise. In all cases, the measurements of intrinsic scatter are robust to the changes in the CMR fit parameters; we find that the differences across all samples and in all bands are significant at the $< 1\sigma$ level.

As a final check on the robustness of the results to the photometric redshift selection, we performed 500 Monte Carlo simulations in which, in addition to the photometry of each object in the catalog being randomized appropriately according to the size of the photometric errors, the photometric redshifts were also re-estimated using EAZY, and the algorithm used to select cluster members described in Section 3.3 was applied. For each of these simulations, the CMR fit parameters and scatter measurements were performed in the manner described above. Again, we found no significant differences from the above results, with the mean slope and intercept of the Monte Carlo simulations being within $< 2\sigma$ of the results for both the photometrically and morphologically selected samples in both z_{850}–J and z_{850}–K_s, and the internal scatter measurements being in agreement across all samples at better than the $< 1\sigma$ level.

Table 2 presents a summary of the measured fit parameters for the z_{850}–J and z_{850}–K_s CMRs, for both the morphologically and photometrically selected samples.

Table 2
CMR Fit Parameters[a]

Color	Mag. Limit[b]	N_g[c]	Slope	Intercept	Offset[d]	σ_{obs}[e]	σ_{int}[f]
Morphologically selected sample (E+S0)							
z_{850}–J	22.5	19	-0.049 ± 0.062	1.335 ± 0.046	-0.005 ± 0.037	0.130 ± 0.047	0.123 ± 0.049
z_{850}–K_s	21.5	16	-0.221 ± 0.057	2.012 ± 0.091	-0.007 ± 0.052	0.177 ± 0.051	0.173 ± 0.052
Photometrically selected sample (all galaxies[g])							
z_{850}–J	24.0	34	-0.112 ± 0.026	1.282 ± 0.016	$+0.014 \pm 0.025$	0.131 ± 0.028	0.118 ± 0.034
z_{850}–K_s	23.0	36	-0.299 ± 0.021	1.914 ± 0.028	-0.003 ± 0.042	0.241 ± 0.035	0.237 ± 0.037

Notes.
[a] Within 0.5 Mpc radius of the cluster X-ray position.
[b] In the redder passband of the color.
[c] Number of galaxies in the subsample.
[d] Biweight location estimate of color offset from the fitted relation.
[e] Biweight scale estimate of scatter about the fitted relation.
[f] Biweight scale estimate of scatter about the fitted relation, corrected for broadening by color errors.
[g] Only objects with $0.8 < z_{850} - J < 1.6$, $1.5 < z_{850}-K_s < 3.0$ (as appropriate) were included in the fit.

4.4. Inferred Ages

The intrinsic scatter about the CMR can be used to estimate the major epoch of star formation for early-type galaxies, given the assumption of a particular stellar population model and that the CMR is predominantly a sequence in metallicity and not age (e.g., Bower et al. 1992). This latter assumption was proven to be sound by observations of the CMR in distant clusters (e.g., Kodama & Arimoto 1997). In actual fact, recent observations have shown that the CMR is primarily a sequence in stellar mass, in that the brightest galaxies tend to be more massive, metal-rich, and older than the galaxies at the faint end of the CMR, with the scatter in the CMR at the faint end being primarily due to differences in age (e.g., Gallazzi et al. 2006).

We modeled the CMR scatter in the manner described by Bower et al. (1992; see also Blakeslee et al. 2003; Mei et al. 2006b). We assumed as our baseline galaxy model a composite stellar population (CSP) of solar metallicity, with Salpeter (1955) IMF, formed in a single burst of star formation, decaying exponentially with characteristic timescale $\tau = 0.1$ Gyr. To check the dependence of our results on the stellar models, we used CSPs derived from Bruzual & Charlot (2003, hereafter BC03, using the Padova 1994 stellar tracks), and Maraston (2005, hereafter M05). One major difference between these two families of models is that the treatment of thermally pulsing asymptotic giant branch (TP-AGB) stars is different, with the M05 models being shown to infer younger ages for galaxies in the Hubble Ultra Deep Field (UDF) in comparison to the BC03 models (Maraston et al. 2006).

We estimate the expected CMR scatter in the following way for each combination of CSP model and photometric bands. We assume that galaxies are born in a single burst of star formation at a time t_{birth} between the epoch of recombination and time t_{end}, where the value of t_{end} is varied in steps between zero and the epoch at which the cluster is observed (i.e., up to a maximum of $t_z \approx 4.3$ Gyr in our adopted cosmology). For each value of t_{end}, we construct a sample of 10,000 simulated galaxies with ages assigned randomly from a uniform distribution with range $0 < t_{birth} < t_{end}$, and estimate the scatter in the color distributions using a biweight scale estimate. The value of t_{end} corresponding to the observed intrinsic CMR scatter is then used to infer estimates of the minimum and mean luminosity-weighted galaxy age assuming a particular CSP.

Figure 7 shows the expected intrinsic scatter σ_{int} around the CMR for the BC03 (red) and M05 (blue) models as a function of minimum age (dashed lines) or mean luminosity-weighted age (solid lines) for the morphologically selected sample. Adopting the BC03 model, the measured intrinsic scatter around the z_{850}–J CMR indicates that the minimum age of the stellar populations of the red sequence galaxies in J2215.9−1738 is $> 1.3 \pm 0.8$ Gyr (corresponding to a minimum redshift of formation of $z_f > 2.1^{+0.7}_{-0.5}$). The corresponding mean luminosity-weighted age is $\overline{t_L} = 2.8 \pm 0.4$ Gyr (i.e., $\overline{z_f} = 4.0^{+1.1}_{-0.7}$). The ages inferred from the M05 model are younger; the minimum age being $> 0.7 \pm 1.6$ Gyr ($z_f > 1.8^{+1.4}_{-0.6}$), and the mean luminosity-weighted age being $\overline{t_L} = 2.5 \pm 0.8$ Gyr ($\overline{z_f} = 3.5^{+2.3}_{-1.0}$). However, the difference between the results for the two different models is not statistically significant.

In z_{850}–K_s, the minimum age is $> 1.6 \pm 0.3$ Gyr ($z_f > 2.4^{+0.3}_{-0.3}$), and the mean luminosity-weighted age is $\overline{t_L} = 3.0 \pm 0.2$ Gyr ($\overline{z_f} = 4.5^{+0.5}_{-0.4}$), assuming the BC03 model. This is in excellent agreement with the age inferred from the scatter about the z_{850}–J CMR, though of course the colors are not completely independent. For the M05 model, we again find lower ages: the minimum age is $> 0.5 \pm 1.2$ Gyr ($z_f > 1.7^{+0.8}_{-0.5}$), and the mean luminosity-weighted age is $\overline{t_L} = 2.4 \pm 0.6$ Gyr ($\overline{z_f} = 3.3^{+1.3}_{-0.7}$).

It is interesting to note that the measured scatter about the z_{850}–K_s CMR is near the limit of the allowed scatter in the M05 model (see Figure 7), although the uncertainty in the measurement is large. In fact, in the case of the photometrically selected sample, the measured scatter is larger than the maximum scatter expected in the M05 model. This could be a consequence of the greater weight given to TP-AGB stars in the M05 models relative to the BC03 models, which begins to have a significant effect at the I band and redder wavelengths (see Figure 18 of Maraston 2005). The observed K_s-band samples the rest-frame z band at the redshift of the cluster.

As the measurements of the intrinsic scatter in z_{850}–J and z_{850}–K_s are consistent between the morphologically and photometrically selected samples (see Section 4.3), the inferred ages derived from the photometrically selected sample are consistent with those quoted above; however, the uncertainties are typically ≈30%–50% smaller due to the increased sample size. We provide a summary of these results in Table 3.

4.5. Dwarf-to-Giant Ratio

Some studies of clusters at high redshift have revealed a deficit in the number of faint red sequence galaxies in comparison

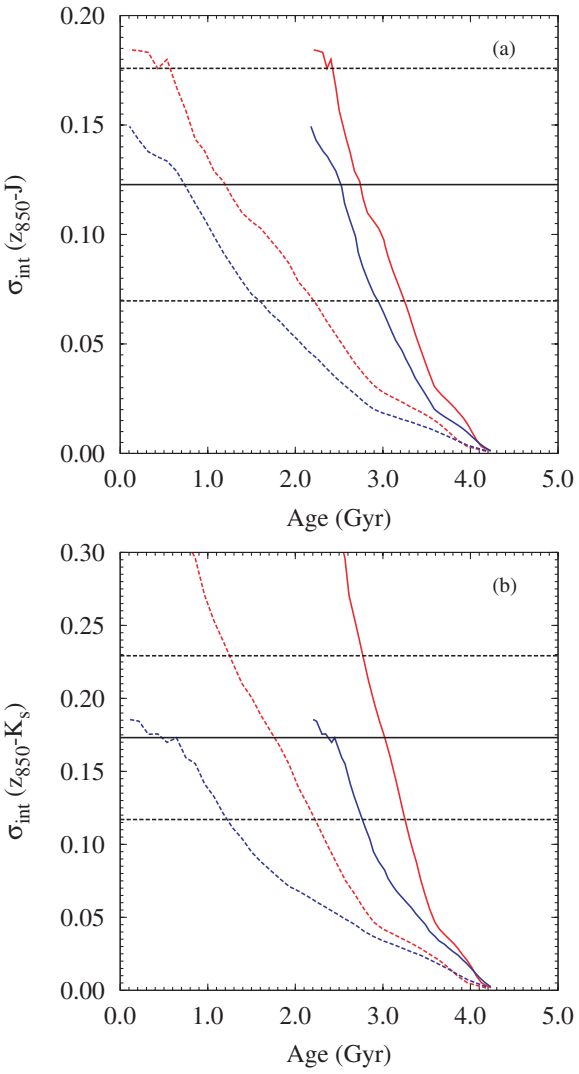

Figure 7. Intrinsic scatter σ_{int} about the CMR vs. age for (*a*) z_{850}–J and (*b*) z_{850}–K_s. The horizontal solid black line indicates the measured value of σ_{int} for the morphologically selected sample of E+S0 galaxies; the horizontal dotted lines indicate the $\pm 1\sigma$ measurement errors in σ_{int}. The solid curves show the mean luminosity-weighted age in the stellar population models used; the dashed curves indicate the corresponding minimum age (red: $\tau = 0.1$ Gyr burst Bruzual & Charlot 2003 model with solar metallicity; blue: equivalent Maraston 2005 model; see Section 4.4 for details).

to observations of clusters at low redshift (e.g., De Lucia et al. 2004, 2007; Stott et al. 2007). This has been attributed to "downsizing", where star formation is observed to have terminated at earlier epochs in more massive galaxies (Cowie et al. 1996). In the case of J2215.9−1738, Figures 5 and 6 show an apparent paucity of galaxies on the red sequence at faint magnitudes ($J > 23.5$), which may be indicative of this phenomenon.

We quantify this deficit using the Dwarf-to-Giant Ratio (DGR). Following De Lucia et al. (2007), we define giants as galaxies with absolute V-band magnitudes brighter than $M_V(\mathrm{Vega}) = -20$, and dwarfs as galaxies fainter than this limit, but brighter than $M_V = (\mathrm{Vega}) = -18.2$. These limits correspond to values at $z = 0$ after correction for the effect of passive evolution. In performing the passive evolution correction, we adopt the same Bruzual & Charlot (2003) simple stellar population model as used by De Lucia et al. (2007), with solar metallicity, Chabrier (2003) IMF, and formation redshift $z_f = 3$. The dividing magnitude between dwarfs and giants is equivalent to $J(\mathrm{AB}) \approx 22.7$ in the observed frame of J2215.9−1738 after this correction is applied, and the corresponding faint magnitude limit is $J(\mathrm{AB}) \approx 24.5$ (see Section 5.3 for details of the adopted conversion between V and J magnitudes). Thus, the faint magnitude limit is ≈0.1 mag fainter than the 5σ limiting magnitude of our observations, and so the limits that we obtain on the DGR may be slightly underestimated in comparison to De Lucia et al. (2007).

We estimated the DGR using the sample of photometrically selected cluster members defined in Section 3.3 and listed in Table 1. Following De Lucia et al. (2007), using all of the members within $r < 0.5R_{200}$ ($R_{200} \approx 0.6$ Mpc for J2215.9−1738; Hilton et al. 2007), we find that the DGR $= 0.50 \pm 0.21$. In estimating the DGR of galaxies on the red sequence, we only consider the z_{850}–J CMR, as unlike the z_{850}–K_s CMR, it is well suited to comparison with other studies at low redshift. Applying a color cut of ±0.3 mag around the fit to the z_{850}–J CMR derived from the morphologically selected sample, we find that the red sequence DGR $= 0.32 \pm 0.18$. The uncertainties are estimated assuming Poissonian errors, added in quadrature to the uncertainty due to the photometric redshift selection, calculated using the full EAZY photometric redshift probability distribution for each galaxy by the same technique described in Section 4.1. The uncertainty due to the photometric redshift selection typically increases the size of the error bars on the DGR measurements by ≈12%.

We checked the sensitivity of these results to the parameters governing the photometric redshift selection. Restricting the membership selection to galaxies with $p_{\Delta_z} > 0.95$ or $1.36 < z_p < 1.56$ does not affect these results significantly, the DGR measurements in each case being well within $< 1\sigma$ of the above results.

Extending the selection radius to $r < 0.75$ Mpc does not change these results significantly: we estimate that the DGR $= 0.65 \pm 0.22$ if all the photometrically selected members are included; if we include only those members within ±0.3 mag of the red sequence, then we find that the DGR $= 0.46 \pm 0.20$.

5. DISCUSSION

5.1. Morphologies

The morphological fractions we find for J2215.9−1738 are in good agreement with studies of clusters at $z \sim 1$, some ∼1.5 Gyr later than the epoch at which our target cluster is observed.

Smith et al. (2005) studied the morphology–density relation in a sample of six clusters at $z \sim 1$. Assuming that $J^* + 1$ is roughly equivalent to the magnitude limit of $M_V^* + 1$ adopted by Smith et al. (2005), as at the redshift of J2215.9−1738 the J-band samples the rest-frame V band, then the depth of our study is sufficient to make a comparison, as all the galaxies in our sample brighter than this limit have morphological classifications (see Figure 5). As Smith et al. (2005) quote their results in bins of local galaxy surface density Σ, we need to estimate the median local galaxy surface density for our sample in order to compare results. Following Smith et al. (2005), we calculate Σ for each galaxy by counting the 10 nearest neighbors with $J < J^* + 1$, and dividing by the rectangular area enclosed. We find the median local galaxy surface density within a radius of 0.5 Mpc of the cluster X-ray position is $\overline{\Sigma} \approx 227$ Mpc^{-2}. In their second highest density bin with $\Sigma > 100$ Mpc^{-2}, Smith et al. (2005) find $f_{\mathrm{E+S0}} = 0.6 \pm 0.1$, in good agreement with the results of our study.

Table 3
Inferred Stellar Population Ages

Color	Model[a]	t_f[b] (Gyr)	z_f[c]	$\overline{t_L}$[d] (Gyr)	$\overline{z_f}$[e]
Morphologically selected sample (E+S0)					
z_{850}–J	BC03	$> 1.3 \pm 0.8$	$> 2.1^{+0.7}_{-0.5}$	2.8 ± 0.4	$4.0^{+1.1}_{-0.7}$
z_{850}–J	M05	$> 0.7 \pm 1.6$	$> 1.8^{+1.4}_{-0.6}$	2.5 ± 0.8	$3.5^{+2.3}_{-1.0}$
z_{850}–K_s	BC03	$> 1.6 \pm 0.3$	$> 2.4^{+0.3}_{-0.3}$	3.0 ± 0.2	$4.5^{+0.5}_{-0.4}$
z_{850}–K_s	M05	$> 0.5 \pm 1.2$	$> 1.7^{+0.8}_{-0.5}$	2.4 ± 0.6	$3.3^{+1.3}_{-0.7}$
Photometrically selected sample (all galaxies[f])					
z_{850}–J	BC03	$> 1.3 \pm 0.5$	$> 2.2^{+0.4}_{-0.3}$	2.8 ± 0.2	$4.1^{+0.7}_{-0.5}$
z_{850}–J	M05	$> 0.8 \pm 0.9$	$> 1.8^{+0.6}_{-0.4}$	2.5 ± 0.4	$3.6^{+1.0}_{-0.6}$
z_{850}–K_s	BC03	$> 1.3 \pm 0.2$	$> 2.1^{+0.2}_{-0.1}$	2.8 ± 0.1	$4.0^{+0.2}_{-0.2}$
z_{850}–K_s	M05	...	...	...	...

Notes. Entries in this table correspond to samples defined in Table 2. The measured internal scatter from the z_{850}–K_s CMR of the photometrically selected sample is out of the range of the M05 model, and so is undefined.
[a] Stellar population model: BC03 = Bruzual & Charlot (2003), M05 = Maraston (2005). See Section 4.4 for details.
[b] Minimum stellar population age at the redshift of J2215.9−1738.
[c] Minimum formation redshift of the stellar population.
[d] Mean luminosity-weighted stellar population age at the redshift of J2215.9−1738.
[e] Mean formation redshift corresponding to mean luminosity-weighted stellar population age.
[f] Only objects with $0.8 < z_{850} - J < 1.6$, $1.5 < z_{850}$–$K_s < 3.0$ (as appropriate) included.

A study of the morphology–density relation at $z \sim 1$ was also conducted by the ACS Guaranteed Time Observations (GTO) team (Postman et al. 2005), who quote morphological fractions within R_{200} for the individual objects that make up their sample. The magnitude limit of the Postman et al. (2005) study is $z_{850} \leqslant 24$, as adopted in this work. For J2215.9−1738, the R_{200} radius is ≈0.6 Mpc (Hilton et al. 2007), i.e., approximately the same as the 0.5 Mpc radius in which we have calculated the morphological fractions. The mean morphological fractions within R_{200} for the Postman et al. (2005) sample (± the standard error on the mean) are $f_{\rm E} = 0.38 \pm 0.03$; $f_{\rm S0} = 0.16 \pm 0.04$; $f_{\rm Sp+Irr} = 0.48 \pm 0.07$; and $f_{\rm E+S0} = 0.55 \pm 0.07$. The results we obtain for J2215.9−1738 are in agreement at the $< 1\sigma$ level for all morphological bins. A larger cluster sample would be needed to search for possible evolutionary effects between $z \sim 1.5$ and $z \sim 1$.

5.2. Inferred Ages

The mean redshift we find for the major epoch of star formation in the early-type galaxies in J2215.9−1738 of $z_f \approx 3$–5 (see Section 4.4) is similar to that found for elliptical galaxies in other high redshift clusters. Mei et al. (2006b) found a mean formation redshift of $z_f \approx 4$ for the elliptical galaxies within 0.5 Mpc radius of the centers of the two Lynx clusters at $z = 1.26$, from modeling the CMR scatter using single burst BC03 models, in good agreement with our result. Similarly, Lidman et al. (2008) conducted a study of the $J - K_s$ CMR in the only other $z > 1.3$ X-ray selected cluster currently known, XMMU J2235.3−2557, finding $z_f \approx 4$ for galaxies, selected using a color cut, within 0.2 Mpc of the cluster center.

For well studied clusters at lower redshift, slightly smaller formation redshifts have been measured from the scatter about the CMR: Blakeslee et al. (2003) estimated $z_f \approx 2.7$ from the i_{775}–z_{850} E+S0 CMR of RDCS J1252.9−2927 at $z = 1.24$, a result also found by Lidman et al. (2004) from the $J - K_s$ CMR; Mei et al. (2006a) found $z_f \approx 3$ from the CMR of elliptical galaxies in RDCS J0910+5422 at $z = 1.10$; and Blakeslee et al. (2006) estimate that the elliptical galaxies in the $z = 0.83$ clusters MS 1054–03 and RX J0152.7−1357 completed their major epoch of star formation at $z_f > 2.2$. All of these studies used BC03 stellar population synthesis models in arriving at their results.

5.3. Evolution of the Color–Magnitude Relation

To compare our measurements of CMR parameters with other studies at lower redshift, we derived linear conversions between observed colors and magnitudes and $U-V$, V (Vega) in the rest frame of the Coma cluster, using $\tau = 0.1$ Gyr Bruzual & Charlot (2003) models of several metallicities ($0.2Z_\odot$, $0.4Z_\odot$, $Z_\odot$, $2.5Z_\odot$), with a range of ages (corresponding to $2 < z_f < 7$, as appropriate for the early-type population, Section 4.4). The method used is the same as that described in Appendix II of Mei et al. (2009), except that we convert magnitudes to V apparent (Vega) at the distance of the Coma cluster. The following transformations were used:

$$(U - V)_{z=0.02} = (1.178 \pm 0.003) \quad (z_{850} - J) - (0.658 \pm 0.005), \tag{5}$$

$$V_{z=0.02} = J - (0.098 \pm 0.003) \quad (z_{850} - J) - (9.455 \pm 0.004). \tag{6}$$

Note that in the following discussion, we only consider the z_{850}–J CMR of J2215.9−1738, as the z_{850}–K_s CMR (roughly equivalent to rest-frame $U-z$) is a poor match to other studies in the literature. As the CMR fitting parameters for J2215.9−1738 derived from the morphologically and photometrically selected samples are consistent, we only quote transformed quantities corresponding to the morphologically selected sample below.

Figure 8 shows the evolution of the intrinsic scatter $\sigma_{\rm int}(U - V)_{z=0.02}$ about the CMR, as traced by studies of several clusters at different redshifts. Some of the studies shown in this plot measured $\sigma_{\rm int}$ through passbands roughly equivalent to $U-V$ at their respective redshifts, and so the correction to $(U - V)_{z=0.02}$ using the models is small. These are the Bower et al. (1992) study of the Coma cluster; the work by Ellis et al. (1997) at $z \approx 0.54$; and the two $z = 0.83$ clusters observed by Blakeslee et al. (2006).

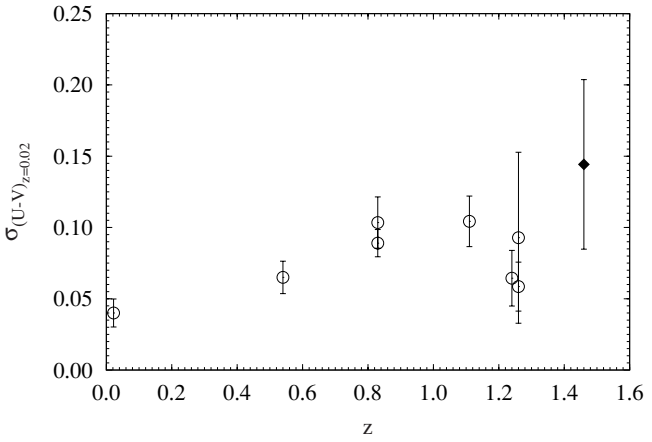

Figure 8. Evolution of the intrinsic scatter around the CMR with redshift in $U-V$ in the rest frame of the Coma cluster (converted from the observed frame using Bruzual & Charlot 2003 models). Open points show values for several clusters in the literature from the works of Bower et al. (1992), Ellis et al. (1997), Blakeslee et al. (2006) (two $z = 0.83$ clusters); Mei et al. (2006a), Blakeslee et al. (2003), Mei et al. (2006b) (two $z = 1.26$ clusters), ordered by increasing redshift. The black diamond marks the value derived from the z_{850}–J CMR of J2215.9−1738 (morphologically selected sample of E+S0 galaxies). The scatter is increasing with redshift, as expected for the passive evolution of a stellar population formed at much higher redshift.

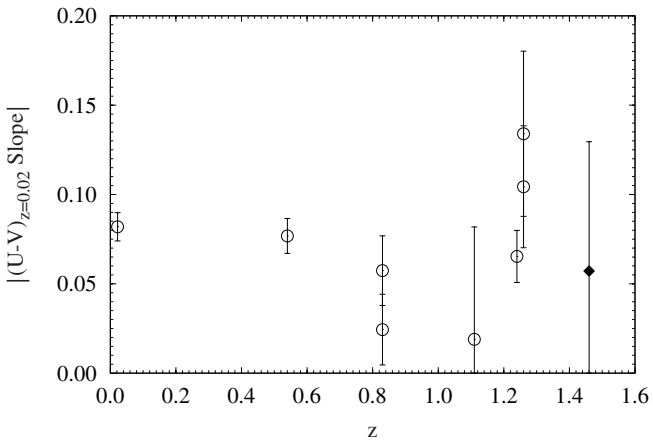

Figure 9. Evolution of the absolute slope of the $U-V$ CMR in the rest frame of the Coma cluster (converted from the observed frame using Bruzual & Charlot 2003 models). Open points show the values for the same comparison sample of clusters drawn from the literature as shown in Figure 8. The black diamond marks the value derived from the z_{850}–J CMR of J2215.9−1738 (morphologically selected sample of E+S0 galaxies). There is no evidence for evolution of the value of the slope with redshift, though the uncertainties in the slope measurements at high redshift are very large.

At $z > 1$, the ACS GTO team measured $\sigma_{\rm int}$ in i_{775}–z_{850}, which is more closely matched to rest-frame $U-B$, and so the transformation of these results to $(U-V)_{z=0.02}$ is larger and more uncertain. Both the Blakeslee et al. (2003) study of RDCS J1252.9−2927 at $z = 1.24$, and the Mei et al. (2006b) study of the Lynx clusters at $z = 1.26$, show similar values of $\sigma_{\rm int}$ to those measured at $z = 0.54$ by Ellis et al. (1997), and $z = 0.83$ by Blakeslee et al. (2006), although the uncertainties are large.

The general trend in Figure 8 is of increasing scatter about the CMR as redshift increases, as expected if the stellar populations were formed at much higher redshifts than observed and have evolved passively thereafter. The intrinsic scatter about the red sequence observed in J2215.9−1738 at $z = 1.46$ is $(U-V)_{z=0.02} = 0.144 \pm 0.059$, more than three times as large as that observed in the Coma cluster (Bower et al. 1992; Eisenhardt et al. 2007), some ∼9 Gyr earlier, and one and a half times that observed in MS 1054−03 and RX J0152.7−1357 at $z = 0.83$, ∼2.2 Gyr earlier.

Figure 9 shows values of the absolute $(U-V)_{z=0.02}$ CMR slope for the same comparison sample of clusters from the literature. In contrast to the measurements of intrinsic scatter about the CMR, we see no evidence for evolution in the slope over the last ∼9 Gyr. For J2215.9−1738, the value of the CMR slope is -0.057 ± 0.072, after conversion to $(U-V)_{z=0.02}$. This agrees with the slope measured for the Coma cluster (Bower et al. 1992; Eisenhardt et al. 2007) at better than the $< 1\sigma$ level, though the uncertainty is large. The lack of evolution of the CMR slope is consistent with the CMR remaining as primarily a sequence in metallicity up to the highest redshifts so far observed.

To compare the evolution of the CMR intercept, we used the CMR of Coma as measured by Bower et al. (1992) to calibrate the CMR as a metallicity sequence, and transformed the CMRs of J2215.9−1738 and the literature comparison sample, such that the intercept was evaluated at the V-band magnitude corresponding to solar metallicity. The metallicity calibration of the CMR of Coma was performed by calculating V-band (Vega) magnitudes corresponding to the $U-V$ colors of $\tau = 0.1$ Gyr BC03 models of several metallicities, assuming the slope and intercept of the Coma CMR as measured by Bower et al. (1992), and formation redshift $z_f = 2$ (Bower et al. 1992). Under these assumptions, solar metallicity in the Coma CMR corresponds to V(Vega) = 13.27. We calculated the corresponding V-band magnitudes and transformed CMR intercepts for the other clusters in the comparison sample assuming passive evolution of this model. Errors in the transformed values were estimated using a Monte Carlo method, taking into account the uncertainties in the measured CMRs, and the color and magnitude transformations to $U - V_{z=0.02}$, V (Vega).

Figure 10 shows the results of this exercise, with the expected passive evolution track of the baseline stellar population model overplotted, for several different formation redshifts. The CMR intercept evaluated at solar metallicity for J2215.9−1738 is consistent with $z_f = 3$, which is slightly lower than the formation redshift inferred from the intrinsic scatter (Section 4.4), but in good agreement given the large uncertainties. This is consistent with the literature comparison sample: there is some scatter, which could indicate a range of star formation histories for the galaxy population in different clusters, but the uncertainties are large. Photometric calibration uncertainties may also contribute to the scatter; see, for example, the discussion in the Mei et al. (2006b) study of the Lynx clusters at $z = 1.26$.

We show the effect of changing the stellar population model from BC03 to M05 on the expected passive evolution of the colors of solar metallicity galaxies in Figure 11. Lower formation redshifts are expected if this family of models is assumed, with some of the literature comparison sample being expected to have formed most of their stars at $z < 2$. In the case of J2215.9−1738, Figure 11 implies $z_f \approx 2$. Again, this is in good agreement with the age derived from the intrinsic scatter about the CMR for the M05 models.

5.4. Dwarf-to-Giant Ratio

The DGR measured for J2215.9−1738 appears to be significantly lower than has been measured in clusters at lower redshifts. De Lucia et al. (2007) quote a red sequence luminous-to-faint ratio within $r < 0.5R_{200}$ for the Coma cluster equivalent

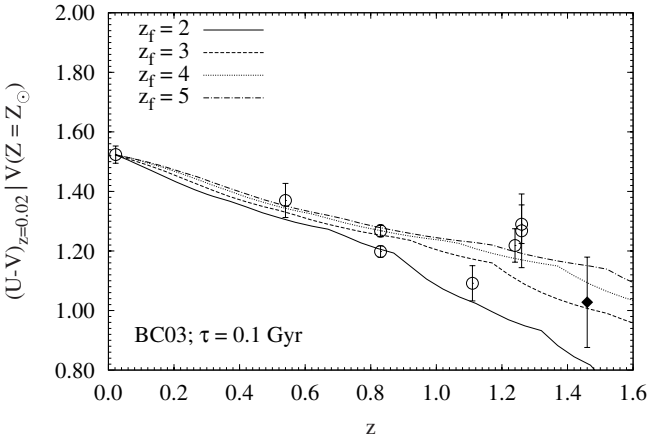

Figure 10. Evolution of the expected $U-V$ color of a galaxy with solar metallicity, in the rest frame of the Coma cluster (converted from the observed frame using Bruzual & Charlot 2003 models), where the Coma CMR has been used to calibrate the CMR as a magnitude–metallicity relation, under the assumption that $z_f = 2$ for Coma. Passive evolution has been taken into account in transforming the CMRs from the literature assuming the same $z_f = 2$ model. The expected passive evolution tracks for several other formation redshifts are also plotted. Open points show the values for the same comparison sample of clusters drawn from the literature as shown in Figure 8. The black diamond marks the value derived from the z_{850}–J CMR of J2215.9−1738 (morphologically selected sample of E+S0 galaxies). The scatter of the data points about the model evolution tracks may indicate variation in the star formation histories of the galaxy populations between clusters.

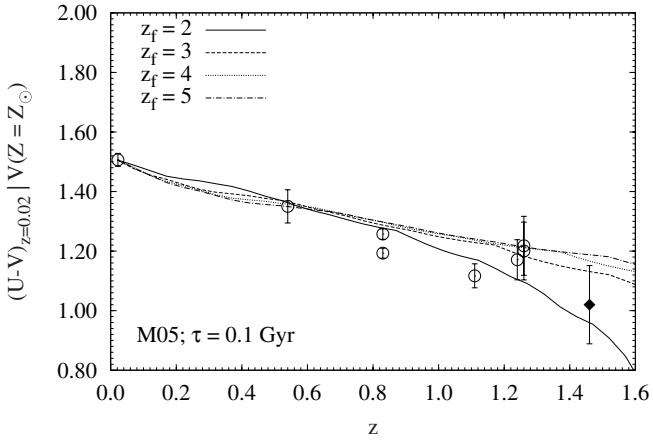

Figure 11. As Figure 10, except the expected evolution of the $U-V$ color at solar metallicity is calculated from the passive evolution of Maraston (2005) $\tau = 0.1$ Gyr burst models.

to a DGR of 3.13 ± 0.59, nearly 10 times the value of the red sequence DGR in J2215.9−1738 (0.32 ± 0.18). Although the DGR we measure is likely to be slightly underestimated, given that our magnitude limit is ≈0.1 mag brighter than the faint magnitude limit adopted by De Lucia et al. (2007), it seems very unlikely that this would be enough to account for the deficit of faint red sequence galaxies relative to Coma.

Several studies at lower redshift have parameterized the evolution of the red sequence DGR with redshift. Recently, Gilbank & Balogh (2008) compiled several measurements of the DGR in clusters at $z < 1$, including studies by Barkhouse et al. (2007), Gilbank et al. (2008), Hansen et al. (2007), De Lucia et al. (2007), and Stott et al. (2007), transformed on to a common system defined by De Lucia et al. (2007), as we have adopted in performing our estimate of the DGR (described in Section 4.5). Gilbank & Balogh (2008) found that the evolution of the DGR with redshift of their composite sample is $\propto (1+z)^{-1.8\pm0.5}$. At the redshift of J2215.9−1738, the expected DGR $= 0.68 \pm 0.36$ from this relation, in good agreement with our estimate of the DGR.

We conclude that J2215.9−1738 appears to show a significant deficit of faint red sequence galaxies compared to clusters in the local universe, and that the measured DGR is of similar magnitude to that expected from extrapolation of the DGR-redshift relation measured at $z < 1$. However, it is known that the cluster-to-cluster scatter of the DGR is considerable (De Lucia et al. 2007), and study of a larger sample of clusters, ideally with large numbers of spectroscopically confirmed members, at similar redshift to J2215.9−1738 is required in order to confirm whether or not this holds for the general population at this epoch.

6. CONCLUSIONS

We have conducted a study of the morphological fractions and CMR in the galaxy cluster XMMXCS J2215.9−1738 at $z = 1.46$. This is the first such study of an X-ray selected cluster at $z \sim 1.5$. We found the following.

1. The brightest members of J2215.9−1738 have K_s magnitudes corresponding to the expected value of $\sim M^*$ in the galaxy luminosity function. This is significantly fainter than the brightest galaxies in the only other $z > 1.3$ X-ray selected cluster studied to date, XMMU J2235.3−2557 at $z = 1.39$ (Lidman et al. 2008).
2. The morphological fractions are $f_{\rm E} = 0.54 \pm 0.17$, $f_{\rm S0} = 0.08 \pm 0.07$, $f_{\rm Sp+Irr} = 0.38 \pm 0.15$, similar to other clusters at $z \sim 1$. Thus, the dominant component of the galaxy population observed in clusters at low redshift was already in place ∼4.5 Gyr after the big bang.
3. After transformation from z_{850}–J to $(U-V)_{z=0.02}$, the slope of the CMR is consistent with that of the Coma cluster, implying little evolution over the last ∼9 Gyr, though the measurement uncertainty is large. In contrast, the intrinsic scatter about the CMR is more than three times the value measured in the Coma cluster, after conversion from z_{850}–J to $(U-V)_{z=0.02}$.
4. From comparison with stellar population models, the intrinsic scatter about the CMR implies mean luminosity-weighted ages for the stellar populations of the early-type galaxies in J2215.9−1738 of ≈3 Gyr, corresponding to the main epoch of star formation in these galaxies coming to an end at $z_f \approx 3$–5. Comparison of the intercept of the CMR with passive evolution of the same stellar population models, calibrated relative to the Coma cluster, yields consistent results.
5. J2215.9−1738 shows evidence of the "downsizing" phenomenon: the red sequence DGR for the cluster is 0.32 ± 0.18 within a radius of $0.5 R_{200}$, although this is likely to be underestimated slightly in comparison to other studies due to the depth of our photometry. This is consistent with extrapolation of the redshift evolution of the DGR measured from cluster samples at $z < 1$ within the large uncertainties.

We thank the referee for a number of suggestions that improved the clarity of this paper. This work is based in part on data collected at the Subaru telescope, which is operated by the National Observatory of Japan, and *XMM-Newton*, an ESA science mission funded by contributions from ESA member states and from NASA. We thank Ichi Tanaka for the development

of the MCSRED package used to reduce the MOIRCS data. We acknowledge financial support from the South African National Research Foundation, the UK Science and Technology Facilities Council, and the University of Sussex Physics & Astronomy Department. Financial support for this work was also provided by NASA through program GO-10496 from the Space Telescope Science Institute, which is operated by AURA, Inc., under NASA contract NAS 5-26555. This work was also supported in part by the Director, Office of Science, Office of High Energy and Nuclear Physics, of the U.S. Department of Energy under Contract AC02-05CH11231, as well as a JSPS core-to-core program "International Research Network for Dark Energy" and by JSPS research grant 20040003. This work was performed under the auspices of the U.S. Department of Energy by Lawrence Livermore National Laboratory in part under Contract W-7405-Eng-48 and in part under Contract DE-AC52-07NA27344. The authors wish to recognize and acknowledge the very significant cultural role and reverence that the summit of Mauna Kea has always had within the indigenous Hawaiian community; we are fortunate to have the opportunity to conduct observations from this mountain.

Facilities: HST, Keck:II, Subaru, VLT:Antu, *XMM-Newton*

REFERENCES

Andreon, S. 2008, MNRAS, 386, 1045
Appenzeller, I., et al. 1998, Messenger, 94, 1
Barkhouse, W. A., Yee, H. K. C., & López-Cruz, O. 2007, ApJ, 671, 1471
Beers, T. C., Flynn, K., & Gebhardt, K. 1990, AJ, 100, 32
Benítez, N. 2000, ApJ, 536, 571
Bertin, E., & Arnouts, S. 1996, A&AS, 117, 393
Blakeslee, J. P., et al. 2003, ApJ, 596, L143
Blakeslee, J. P., et al. 2006, ApJ, 644, 30
Blanton, M. R., & Roweis, S. 2007, AJ, 133, 734
Bower, R. G., Lucey, J. R., & Ellis, R. S. 1992, MNRAS, 254, 601
Brammer, G. B., van Dokkum, P. G., & Coppi, P. 2008, ApJ, 686, 1503
Bruzual, G., & Charlot, S. 2003, MNRAS, 344, 1000
Casertano, S., et al. 2000, AJ, 120, 2747
Chabrier, G. 2003, PASP, 115, 763
Collins, C. A., et al. 2009, Nature, 458, 603
Collister, A. A., & Lahav, O. 2004, PASP, 116, 345
Cowie, L. L., Songaila, A., Hu, E. M., & Cohen, J. G. 1996, AJ, 112, 839
Crawford, S. M., Bershady, M. A., & Hoessel, J. G. 2009, ApJ, 690, 1158
Dawson, K. S., et al. 2008, AJ, submitted
De Lucia, G., & Blaizot, J. 2007, MNRAS, 375, 2
De Lucia, G., et al. 2004, ApJ, 610, L77
De Lucia, G., et al. 2006, MNRAS, 366, 499
De Lucia, G., et al. 2007, MNRAS, 374, 809
De Propris, R., et al. 1999, AJ, 118, 719
Dressler, A., et al. 1997, ApJ, 490, 577
Eisenhardt, P. R., et al. 2007, ApJS, 169, 225
Eisenhardt, P. R. M., et al. 2008, ApJ, 684, 905
Ellis, R. S., et al. 1997, ApJ, 483, 582
Faber, S. M., et al. 2003, Proc. SPIE, 4841, 1657
Feldmann, R., et al. 2006, MNRAS, 372, 565
Fioc, M., & Rocca-Volmerange, B. 1997, A&A, 326, 950
Ford, H. C., et al. 2003, Proc. SPIE, 4854, 81
Gallazzi, A., Charlot, S., Brinchmann, J., & White, S. D. M. 2006, MNRAS, 370, 1106
Gilbank, D. G., & Balogh, M. L. 2008, MNRAS, 385, L116
Gilbank, D. G., et al. 2008, ApJ, 673, 742
Hansen, S. M., Sheldon, E. S., Wechsler, R. H., & Koester, B. P. 2007, arXiv:0710.3780
Hilton, M., et al. 2007, ApJ, 670, 1000
Holden, B. P., et al. 2005, ApJ, 620, L83
Holden, B. P., et al. 2006, ApJ, 642, L123
Holden, B. P., et al. 2007, ApJ, 670, 190
Ichikawa, T., et al. 2006, Proc. SPIE, 6269, 626916
Jørgensen, I., et al. 2006, ApJ, 639, L9
Kodama, T., & Arimoto, N. 1997, A&A, 320, 41
Larson, R. B. 1974, MNRAS, 169, 229
Lidman, C., et al. 2004, A&A, 416, 829
Lidman, C., et al. 2008, A&A, 489, 981
Maraston, C. 2005, MNRAS, 362, 799
Maraston, C., et al. 2006, ApJ, 652, 85
McCarthy, P. J., et al. 2007, ApJ, 664, L17
Mei, S., et al. 2009, ApJ, 690, 42
Mei, S., et al. 2006a, ApJ, 639, 81
Mei, S., et al. 2006b, ApJ, 644, 759
Menci, N., et al. 2008, ApJ, 685, 863
Mullis, C. R., et al. 2005, ApJ, 623, L85
Oke, J. B. 1974, ApJS, 27, 21
Postman, M., et al. 2005, ApJ, 623, 721
Romer, A. K., Viana, P. T. P., Liddle, A. R., & Mann, R. G. 2001, ApJ, 547, 594
Sahlén, M., et al. 2009, MNRAS, in press (arXiv:0802.4462)
Salpeter, E. E. 1955, ApJ, 121, 161
Schlegel, D. J., Finkbeiner, D. P., & Davis, M. 1998, ApJ, 500, 525
Smith, G. P., et al. 2005, ApJ, 620, 78
Stanford, S. A., Eisenhardt, P. R., & Dickinson, M. 1998, ApJ, 492, 461
Stanford, S. A., et al. 2005, ApJ, 634, L129
Stanford, S. A., et al. 2006, ApJ, 646, L13
Stott, J. P., et al. 2007, ApJ, 661, 95
Tanaka, M., et al. 2005, MNRAS, 362, 268
Tanaka, M., et al. 2008, A&A, 489, 571
Tinsley, B. M. 1978, ApJ, 222, 14
Tokunaga, A. T., & Vacca, W. D. 2005, PASP, 117, 421
van der Wel, A., et al. 2007, ApJ, 670, 206
van Dokkum, P. G., & Stanford, S. A. 2003, ApJ, 585, 78
van Dokkum, P. G., & van der Marel, R. P. 2007, ApJ, 655, 30
van Dokkum, P. G., et al. 2000, ApJ, 541, 95
van Dokkum, P. G., et al. 2001, ApJ, 552, L101
Wilson, G., et al. 2008, arXiv:0810.0036